Universidade de Aveiro Departamento de Física,
2018

Luísa Madail Pimentel

Estados topologicamente protegidos na rede de Lieb

Topologically protected states in the Lieb lattice

Luísa Madail Pimentel

Estados topologicamente protegidos na rede de Lieb

Topologically protected states in the Lieb lattice

Dissertação apresentada à Universidade de Aveiro para cumprimento dos requisitos necessários à obtenção do grau de Mestre em Engenharia Física, realizada sob a orientação científica do Doutor Ricardo Assis Guimarães Dias, professor auxiliar do Departamento de Física da Universidade de Aveiro.

o júri / the jury

presidente / president

Margarida Maria Resende Vieira Facão
Professora auxiliar da Universidade de Aveiro

vogais / examiners committee

Pedro José Gonçalves Ribeiro
Professor auxiliar do Instituto Superior Técnico

Ricardo Assis Guimarães Dias
Professor auxiliar da Universidade de Aveiro (orientador)

acknowledgements

I take this opportunity to express my gratitude to my supervisor Dr. Ricardo Dias for providing me with the possibility and tools to understand and accomplish this thesis on *topologically protected states in the Lieb lattice*. I am extremely grateful for his guidance, invaluable constructive criticism and encouragement throughout the course of this thesis.
Also, I would like to thank Dr. Andrew Daley for receiving me in his research group and for all the insight given during the early stages of this dissertation. Furthermore, I thank my family and friends for their assistance and support during my academic path and I would also like to extend my sincere regards for the teaching staff of the Department of Physics for their support and friendly advice.

Abstract

In this thesis, we study the different types of boundary modes found in Lieb-type tight-binding Hamiltonians (of chains, ribbons and square clusters) that are strongly dependent on the symmetries present in the lattice. A new topological description is developed, with the aim of predicting the behaviour of these edge states.

Due to the unconventional symmetry features of the Lieb unit cell, a generalization of the Zak's phase invariant and the chiral pairing operation is realized and implemented to sustain our topological characterization.

Our analysis reveals that, while a large set of boundary states have a common well defined topological phase transition, other edge states reflect a topological non-trivial phase for any finite value of the hopping parameters and are responsible for the appearance of corner states in the two dimensional Lieb rotated square lattice when reaching a higher symmetry class.

The introduction of symmetry preserving local onsite potentials in these Lieb-type systems lifts the "degeneracy" of the topological transition point, inducing a "cascade" of topological transitions. This feature is enhanced with increasing lattice spatial dimensions.

Resumo

A presente dissertação tem como objetivo estudar os diferentes estados de fronteira existentes em Hamiltonianos de *tight-binding* de sistemas baseados na rede de Lieb, com grande dependência na simetria do sistema. No decurso da tese, uma descrição topológica é desenvolvida com o propósito de prever o comportamento destes estados fronteira.

Devido às características pouco convencionais de simetria na célula unitária da rede de Lieb, foram formuladas generalizações do invariante topológico baseado na fase de Zak e da operação de emparelhamento quiral de estados, posteriormente implementadas de modo a sustentar a caracterização topológica dos sistemas estudados.

A análise revela a existência de estados de fronteira com uma transição de fase topológica bem definida e outros que refletem uma fase topológica não-trivial para qualquer escolha de parametros de salto. Estes últimos, são responsáveis pela criação de estados de canto na rede quadrada de Lieb rodada quando uma classe de simetria superior é alcançada.

A partir da introdução de potenciais locais que preservam a simetria nos sistemas baseados na rede de Lieb, a "degenerescência" do ponto de transição topológica é levantada, induzindo uma "cascata" de transições topológicas. Este efeito é otimizado pelo aumento das dimensões espaciais do sistema.

Contents

List of Figures

Chapter 1
Introduction

In recent years relevant advances have been done in the understanding of topological states of quantum matter, particularly for the investigation of insulating and semi-metallic electronic structures, superconductors and interacting bosonic and fermionic systems. The rise of new physical phenomena revealed promising applications in spintronics, quantum information processing and high efficiency magnetoelectric devices [1]. The major feature of topological materials has to do with the manifestation of protected surface states arising from the exotic bulk phenomena [2]. Materials classified as topological insulators behave as ordinary insulators in its bulk while as a metal on its boundary [3, 4, 5, 6, 7]. The bulk of these materials has an energy gap separating the highest occupied electronic band from the lowest empty band. However, near its boundary, surface states exist within the gap of bulk bands. This leads to itinerant electrons near the edges reflecting a series of edge-conducting channels. These characteristics can be experimentally found, for instance, in the one-dimensional polyacetylene discovered in 1979 [8], two dimensional HgTe/CdTe quantum well in 2007 [9, 10] and InAs/GaSb quantum well in 2011 [11], and three-dimensional Bi_2Se_3, Bi_2Te_3 and Sb_2Te_3 in 2009 [12].

As a means of characterizing an insulating Hamiltonian, researchers commonly employ the conception of topological invariant, an integer number measuring the global phase structure of the bulk wave functions. There are two classes of topological invariants for topological insulators: the elements of group Z which collects all integers such as the integer quantum Hall effect, characterized by the n filling factor of electrons and the elements of group Z_2 consisting of $\{0, \pm 1\}$ values which, in a 3D topological insulator with time reversal symmetry, 0 and 1 represent the existence of odd and even numbers of surface states, respectively [13]. In many cases, the calculation of the mathematical definitions of the topological invariants for realistic models is not straightforward. Nevertheless, one may rely on the idea that a smooth deformation implying a change in the Hamiltonian without closing the bulk gap maintains its topological phase. Thus, starting with an inversion-symmetric crystal structure for which the Z_2 topological invariants can easily be computed, and then smoothly transform into the structure of interest, one can expect that the Z_2 topological class will still be admissible [14]. The conservation of the topological phase when the band structure remains gapped suggests that two quantum systems belonging to different topological classes in contact with each other must support gapless states [15]. In the physics field, quantized quantities such as the Hall conductance also have a topological origin and remain unchanged by small changes in the sample. The topological order can be understood in the sense that certain fundamental properties (such as the Hall conductance) are insensitive to small changes in material parameters and cannot change unless the system goes through a quantum phase transition between topologically different phases.

The topological invariant allows for the determination of the nontrivial phase of a given system, which in turn enables the connection between topological invariants that characterize the bulk momentum-space Hamiltonian of an infinite model and the appearance of edge states in the respective open system. Such procedure is frequently denominated as bulk-boundary correspondence. We have stated that a topological phase transition is followed by the closing of a gap in the band structure of a given system. In this process, the role of symmetry is crucial. In fact, when introducing a sublattice potential breaking the chiral symmetry, it is

possible to adiabatically deform the Su-Schrieffer-Heeger model into a topologically trivial state without closing the bulk gap and the topological identification no longer holds [16]. For this reason, topological insulators are said to have symmetry-protected topological order (SPT) [2]. Topological states can then be protected by nonspatial symmetries such as time-reversal, particle-hole and chiral symmetry as well as spatial lattice symmetries, often related to crystals as point-group symmetries, which involve transformations that preserve a spatial point, namely, inversion, rotation and reflection operations. Any symmetry transformation can be represented by an operator in the Hilbert space. For spatial symmetries, the transformation depends on the lattice site labels while the nonspatial transformation acts on each lattice site separately.

The theoretical study of topological phases of matter and the strong correlation with non-spatial symmetries gave rise to the development of a topological classification framework, namely, the periodic table of topological insulators (TI) and superconductors (TSC) [17]. This classification categorizes quadratic Hamiltonians with a given set of non-spatial symmetries into topological equivalence classes. The determination of these classes according to Cartan-Altland-Zirnbauer classification scheme [18] relies on systems whose irreducible Hamiltonians do not exhibit unitary symmetries and evaluates the possible outcomes of the symmetry transformation acting on a given Hamiltonian in first quantization. Thus, (see Table 1.1) for both time-reversal (TRS) and particle-hole (PHS) symmetry, the Hamiltonian can be invariant (represented by 0) or exhibit such symmetry in a way that the operator squares to either ± 1. Under chiral symmetry, the product $S = T \cdot C$ is fully defined by TRS and PHS unless both T and C vanish, in which case we must consider the absence or presence of S.

Class/d	T	C	S	0	1	2	3	4	5	6	7
A	0	0	0	$\mathbb{Z}$	0	$\mathbb{Z}$	0	$\mathbb{Z}$	0	$\mathbb{Z}$	0
AIII	0	0	1	0	$\mathbb{Z}$	0	$\mathbb{Z}$	0	$\mathbb{Z}$	0	$\mathbb{Z}$
AI	+	0	0	$\mathbb{Z}$	0	0	0	$2\mathbb{Z}$	0	$\mathbb{Z}_2$	$\mathbb{Z}_2$
BDI	+	+	1	$\mathbb{Z}_2$	$\mathbb{Z}$	0	0	0	$2\mathbb{Z}$	0	$\mathbb{Z}_2$
D	0	+	0	$\mathbb{Z}_2$	$\mathbb{Z}_2$	$\mathbb{Z}$	0	0	0	$2\mathbb{Z}$	0
DIII	–	+	1	0	$\mathbb{Z}_2$	$\mathbb{Z}_2$	$\mathbb{Z}$	0	0	0	$2\mathbb{Z}$
AII	–	0	0	$2\mathbb{Z}$	0	$\mathbb{Z}_2$	$\mathbb{Z}_2$	$\mathbb{Z}$	0	0	0
CII	–	–	1	0	$2\mathbb{Z}$	0	$\mathbb{Z}_2$	$\mathbb{Z}_2$	$\mathbb{Z}$	0	0
C	0	–	0	0	0	$2\mathbb{Z}$	0	$\mathbb{Z}_2$	$\mathbb{Z}_2$	$\mathbb{Z}$	0
CI	+	–	1	0	0	0	$2\mathbb{Z}$	0	$\mathbb{Z}_2$	$\mathbb{Z}_2$	$\mathbb{Z}$

Table 1.1: Tenfold classification of gapped bulk topological insulators and superconductors. Left column denotes the symmetry classes of fermionic Hamiltonians categorized by the absence (0) or presence (+,–,1) of time-reversal (T), particle-hole (C) and chiral (S) symmetry. These classes are evaluated for the existence of non-trivial topological phases and the correspondent types ($\mathbb{Z}$, $2\mathbb{Z}$, $\mathbb{Z}_2$) of TI/TSC with space dimension d. Adapted from [2].

For a given symmetry class in a given dimension, Table.1.1 evaluates the presence of topological insulators or superconductors and if exists, then $\mathbb{Z}$ (integer number), $2\mathbb{Z}$ (even integer number) and $\mathbb{Z}_2$ (binary quantity) denotes a specific type of value taken from the calculation of the topological invariant that relies on a well quantized physical observable. For instance, in odd dimensions and for the chiral symmetric class AIII a $\mathbb{Z}$-TI/TSC arises and the topological invariant relies on the quantized value of the bulk Hamiltonian winding number corresponding to the number of topologically protected gapless surface modes [19].

Introducing additional spatial symmetries into the previous approach may result in the expansion of the tenfold equivalence classes with the creation of new topological phases. Alternatively, in some cases these spatial symmetries do not change the topological classification

but instead lead to a simplification in the topological invariant calculation for a given class. This is the case of a 3D topological insulator where the $\mathbb{Z}_2$ invariant, in the presence of inversion symmetry, is easily evaluated using the parity values of the time-reversal invariant k-points [20]. The existence of surface modes is also restricted by the spatial symmetries and the bulk-boundary correspondence in this case is not solely supported by the presence of a gapped bulk Hamiltonian. Instead, it also relies on whether the boundaries are left invariant under the spatial symmetries [2].

To date, the quantization of topological invariants for TIs lies in the assumption of certain robust characteristics of the bulk Hamiltonian. Precisely, bands with non-quantized topological indices are known not to sustain surface states lying in the bulk gap. In the present work, we introduce the Lieb lattice as a system which does not exhibit the conceived quantized topology yet features robust boundary modes. More specifically, we theoretically present a generalization of the implemented topological quantities with the purpose of including these type of models into the topological insulators classification.

In this thesis, we start by discussing two particular symmetries hidden in the Lieb lattice - the non-spatial chiral symmetry and the point inversion symmetry - and present a generalized conjecture with the purpose of including systems exhibiting these symmetries in a non-conventional manner (Chapter 2). Particularly, we deal with non-centred inversion symmetric models that have non-symmetric energy chiral-like pairs together with non-zero energy edge states, properties found in the Lieb lattice. In Chapter 3, we introduce the band structure of the two dimensional Lieb lattice and study the appearance of localized edge and plaquette states when open boundary conditions are considered. Subsequently, we propose a modified version of the Lieb lattice exhibiting promising topological phase transitions resulting from the symmetry modifications of the system. With the aim of analysing the different types of boundary states arising from these new topological features, Chapter 4 focus on a lower-dimensional system based on the Lieb unit cell - the Lieb rhombi chain - where we discuss the presence of edge states using the generalized methods of Chapter 2 and the relevance of open boundary conditions employing the bulk-boundary correspondence approach. Finally, in Chapter 5 we consecutively increase the complexity of the rhombi chain, in terms of the size of the unit cell and the implementation of periodic boundary conditions, in order to resolve the 2D proposed system and determine the general characteristics of the boundary modes.

Chapter 2
Symmetry Characterization

Nontrivial topologies in band structures are a consequence of symmetries found in tight-binding systems. For example, magnetic insulators in 2D exhibit the integer quantum Hall effect in the absence of an external magnetic field and this nontrivial topology is characterized by the Chern number, a topological invariant that remains constant unless the charge conservation symmetry is broken. For time-reversal symmetric insulators, the Zak's phase ($\mathcal{Z}_2$) is used to indicate changes within the band structure of the system, more specifically, if the system remains gapped or ungapped [21, 22, 2].

In this chapter we discuss in detail the topological characterization of the SSH model and extend this characterization to one-dimensional models that do not conventionally possess chiral symmetry or that have non-centered inversion symmetry. This overview will be relevant for the further research of the Lieb rhombi chain in chapter 4.

2.1 Inversion-symmetric systems

In the following section we review that, in the presence of inversion symmetry, the Zak's topological invariant can be deduced from the knowledge of the parity eigenvalues of the time-reversal invariant points in the Brillouin zone [20]. In turn, this provides a simple method for determining the topological phase of any inversion-symmetric system and can be used to predict the presence of boundary states for open boundary conditions (OBC) that do not break this symmetry.

For continuous wavefunctions $\Psi(r)$, an inversion operation ($\hat{\Pi}$) about the origin is a transformation $\hat{\Pi}\Psi(r) = \Psi(-r)$. From this unitary operator we acknowledge the properties

$$\hat{\Pi}^2 = 1 \qquad \hat{\Pi}e^{ikr} = e^{-ikr}. \tag{2.1}$$

A Hamiltonian is said to have inversion symmetry if the transformation $\hat{\Pi}\hat{H}\hat{\Pi}^\dagger = \hat{H}$ is verifiable.

When using the inversion operator in finite lattice models, we have to take into account that the edges may break inversion symmetry and therefore we only act on the bulk of such systems. The action of the inversion operation in the momentum space of a bulk Hamiltonian reads

$$\hat{\Pi}\,|\psi_j(k)\rangle = \hat{\Pi}(|k\rangle \otimes |u_j(k)\rangle) = |-k\rangle \otimes \hat{\pi}\,|u_j(k)\rangle \tag{2.2}$$

where $\hat{\pi}$ acts on the internal Hilbert space, $\mathcal{H}_{int}$, of each unit cell, m, composing the system and $|\psi_j(k)\rangle$ is the Bloch eigenstate of band j corresponding to the tensor product of the plane wave $|k\rangle = \frac{1}{\sqrt{N}}\sum_{m=1}^{N} e^{imk}\,|m\rangle$ and the eigenstate of the k-space bulk Hamiltonian $|u_j(k)\rangle$. The lattice model has bulk inversion symmetry if there exists a unitary and hermitian operator $\hat{\pi}$ acting on $\mathcal{H}_{int}$ such that $\hat{\pi}H(-k)\hat{\pi} = H(k)$ and $\hat{\pi}^2 = \hat{1}_{int}$.

If all occupied bands can be adiabatically separated in energy such that we can focus on the wavefunction of a single band, the inversion operation in this state, under a phase degree of freedom, is given by

$$|u(-k)\rangle = e^{i\theta}\hat{\pi}\,|u(k)\rangle \tag{2.3}$$

It is interesting to look at points in the Brillouin Zone (BZ) which map unto themselves under inversion - the so called Time-Reversal Invariant Momenta (TRIM). In d dimensions, there

are 2^d symmetry points at the centre and edges of the BZ [16]. In the one-dimensional case, these points correspond to $k = 0$ and $k = \pi$ and they exhibit a well defined parity given by

$$\hat{\pi}\,|u(0)\rangle = p_0\,|u(0)\rangle \qquad\qquad \hat{\pi}\,|u(\pi)\rangle = p_\pi\,|u(\pi)\rangle \tag{2.4}$$

where $\{p_0, p_\pi\} = \pm 1$.

2.1.1 Zak's phase definition

The topological characterization of one-dimensional lattice systems often relies on the calculation of the Zak's phase, which gives a quantized value of $\{0, \pi\}$ for a given occupied band allowing for the determination of the non trivial topological regimes. This topological invariant is frequently defined as the total phase for a given band j of the Wilson loop ($\mathcal{W}$) – arising from gauge theory to represent parallel transport maps [23] and also used to interpret certain phenomena such the macroscopic polarization in crystalline dielectrics [24] in which we can define an operator of the Wilson loop entirely crossing the Brillouin zone such that the phases of the respective eigenvalues work up to the Wannier centers giving the charge positions with respect to the unit cell [25, 26, 27].

In the tight-binding approximation the discretized Wilson loop of a single band j corresponding to an inversion-symmetric 1D Hamiltonian is expressed as [28, 16]

$$\mathcal{W}_j = \prod_{n=0}^{N-1} \langle u_j(-\pi + n\delta k)\,|\,u_j(-\pi + (n+1)\delta k)\rangle\,. \tag{2.5}$$

with $\delta k = 2\pi/N$ considering we have N sites in the periodic model. Using the relation in Eq.2.3 for band j, we may write $\mathcal{W}_j$ as

$$\begin{aligned}
\mathcal{W}_j = {} & \langle u_j(-\pi)\,|\,u_j(-\pi+\delta k)\rangle\,\langle u_j(-\pi+\delta k)\,|\,u_j(-\pi+2\delta k)\rangle\,... \\
& ...\,\langle u_j(-\delta k)\,|\,u_j(0)\rangle\,\langle u_j(0)\,|\,u_j(\delta k)\rangle\,...\,\langle u_j(\pi-2\delta k)\,|\,u_j(\pi-\delta k)\rangle\,\langle u_j(\pi-\delta k)\,|\,u_j(\pi)\rangle = \\
= {} & \langle u_j(\pi)\,|e^{i\theta_{\pi-\delta k}}\hat{\pi}|\,u_j(\pi-\delta k)\rangle\,\langle u_j(\pi-\delta k)\,|\hat{\pi}e^{-i\theta_{\pi-\delta k}}e^{i\theta_{\pi-2\delta k}}\hat{\pi}|\,u_j(\pi-2\delta k)\rangle\,... \\
& ...\,\langle u_j(\delta k)\,|\hat{\pi}e^{-i\theta_{\delta k}}|\,u_j(0)\rangle\,\langle u_j(0)\,|\,u_j(\delta k)\rangle\,...\,\langle u_j(\pi-2\delta k)\,|\,u_j(\pi-\delta k)\rangle\,\langle u_j(\pi-\delta k)\,|\,u_j(\pi)\rangle\,.
\end{aligned} \tag{2.6}$$

Applying the properties given in Eq.2.1 and Eq.2.4 gives

$$\begin{aligned}
\mathcal{W}_j = {} & \langle u_j(\pi)\,|\hat{\pi}|\,u_j(\pi-\delta k)\rangle\,\langle u_j(\pi-\delta k)\,|\,u_j(\pi-2\delta k)\rangle\,... \\
& ...\,\langle u_j(\delta k)\,|\hat{\pi}|\,u_j(0)\rangle\,\langle u_j(0)\,|\,u_j(\delta k)\rangle\,...\,\langle u_j(\pi-2\delta k)\,|\,u_j(\pi-\delta k)\rangle\,\langle u_j(\pi-\delta k)\,|\,u_j(\pi)\rangle = \\
& = \langle u_j(\pi)\,|\hat{\pi}|\,u_j(\pi-\delta k)\rangle\,\langle u_j(\delta k)\,|\hat{\pi}|\,u_j(0)\rangle = p_0 p_\pi = \pm 1,
\end{aligned} \tag{2.7}$$

which are the two possible values for $\mathcal{W}_j$ for a system with well-defined parity values and large N. This result gives a direct way to analyse the possible values of the Wilson loop for a specific band j if we have the information about the eigenfunctions $|u_j(k)\rangle$ for $k = \{0, \pi\}$.

Let us recall Eq.2.5. For small steps of δk such that we may use the first order Taylor series approximation $|u_j(k-\delta k)\rangle = |u_j(k)\rangle - \delta k \frac{d}{dk}|u_j(k)\rangle$, each term in $\mathcal{W}_j$ can be rewritten using the first order exponential series as

$$\langle u_j(k)\,|\,u_j(k-\delta_k)\rangle \simeq 1 - i\theta_k \simeq e^{-i\theta_k} \tag{2.8}$$

with $\theta_k = -i\delta k\,\langle u_j(k)|\,\dfrac{d}{dk}\,|u_j(k)\rangle$. From this, the Wilson loop simply becomes

$$\mathcal{W}_j = e^{i\sum_{l=0}^{N-1}(i\delta k\langle u_j(k)|\frac{d}{dk}|u_j(k)\rangle)} = e^{i\mathcal{Z}_j}. \tag{2.9}$$

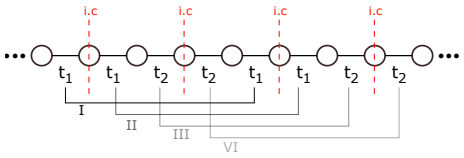

Figure 2.1: $t_1t_2t_2t_1$ chain with inversion axis (i.c) drifted from the center of the unit cells I, II, III and VI.

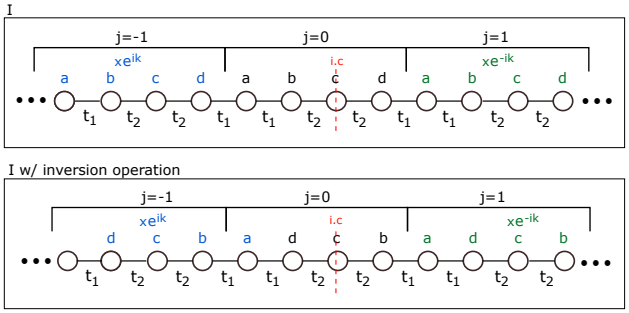

Figure 2.2: Inversion operation in the $t_1t_2t_2t_1$ chain. Index j denotes the unit cell. Upon inversion, the site a within unit cell $j = 0$ will gain k-dependence.

In this way, we arrive at the general expression of the Zak's phase for band j, directly related to the Wilson loop in the form

$$\mathcal{Z}_j = i\int_{-\pi}^{\pi} dk\, \langle u_j(k)\,|\frac{d}{dk}|\,u_j(k)\rangle = \arg(\lim_{N\to\infty} \mathcal{W}_j), \tag{2.10}$$

where we have considered the continuous limit $\delta k \to 0$. We showed that an inversion-symmetric system has a well-quantized Zak's phase of $\mathcal{Z}_j = \{0, \pi\}$ given by the parity of the occupied Bloch wave functions at the time-reversal invariant points in the Brillouin zone [20]. The phase of the Bloch functions can always be chosen such that the Wannier function is even or odd around the centres $x = 0, a/2$ (where a is the lattice constant), giving a well quantized Zak's phase [29]. Moreover, the total phase value of all occupied bands gives information about whether we are in the presence of a trivial or non-trivial system. Therefore, this quantity can be applied for better understanding of the topology of energy bands.

2.1.2 Non-centralized inversion symmetry axis

Not all one-dimensional lattice models with inversion symmetry will display a quantized Zak's phase when applying the previous result of Eq.2.10. This is the case of the Lieb rhombi lattice treated in Chapter 4. Nevertheless, the presence of symmetry protected boundary states leads us to believe these systems have non trivial topology of the bulk wavefunctions, thus we may still define a topological invariant in these circumstances.

The key factor for the non-quantized Zak's phase is that the inversion operator for these systems acquires k-dependent matrix elements. This happens because the middle point of any given choice of unit cell does not meet the inversion centre. For these 1D models, to preserve the quantized values of the topological invariant requires the addition of a correction term in Eq.2.10.

In the following case of the periodic $t_1t_1t_2t_2$ chain in Fig.2.1 the inversion centres do not lie in the middle of each choice of the four possible unit cells (I,II,III,VI). Let us address the case of the unit cell given by I and perform an inversion operation in the system (see Fig.2.2). In this operation, there are overlaps between unit cells and the new non-hermitian inversion operator is forced to have components that depend on k, given by

$$\hat{\Pi}\,|k\rangle \otimes |u_j\rangle = \hat{\Pi}_k\,|u_j(k)\rangle = \begin{bmatrix} e^{ik} & 0 & 0 & 0 \\ 0 & 0 & 0 & 1 \\ 0 & 0 & 1 & 0 \\ 0 & 1 & 0 & 0 \end{bmatrix} \begin{pmatrix} u_a(k) \\ u_b(k) \\ u_c(k) \\ u_d(k) \end{pmatrix}. \tag{2.11}$$

Previously, in order to obtain the Zak's phase from the Wilson loop description we made use of the property $\hat{\Pi}^2 = \hat{1}$. In this case, the Bloch state phase is not constant within the unit cell and

$$\hat{\Pi}^{\dagger}_{k1}\hat{\Pi}_{k2} = \begin{bmatrix} e^{-ik_1} & 0 & 0 & 0 \\ 0 & 0 & 0 & 1 \\ 0 & 0 & 1 & 0 \\ 0 & 1 & 0 & 0 \end{bmatrix} \begin{bmatrix} e^{ik_2} & 0 & 0 & 0 \\ 0 & 0 & 0 & 1 \\ 0 & 0 & 1 & 0 \\ 0 & 1 & 0 & 0 \end{bmatrix} = \begin{bmatrix} e^{-i(k_1-k_2)} & 0 & 0 & 0 \\ 0 & 1 & 0 & 0 \\ 0 & 0 & 1 & 0 \\ 0 & 0 & 0 & 1 \end{bmatrix}, \tag{2.12}$$

which in the first order approximation of the exponential expansion we write the latter product as

$$\hat{\Pi}^{\dagger}_{k1}\hat{\Pi}_{k2} = \hat{1} + i(k_2 - k_1) \begin{bmatrix} 1 & 0 & 0 & 0 \\ 0 & 0 & 0 & 0 \\ 0 & 0 & 0 & 0 \\ 0 & 0 & 0 & 0 \end{bmatrix}. \tag{2.13}$$

The Wilson loop for this system is given by Eq.2.6 with the introduction of the k-dependent inversion operations such that

$$\begin{aligned} \mathcal{W}_j = &\langle u_j(-\pi)\,|\,u_j(-\pi+\delta k)\rangle \langle u_j(-\pi+\delta k)\,|\,u_j(-\pi+2\delta k)\rangle ... \\ &... \langle u_j(-\delta k)\,|\,u_j(0)\rangle \langle u_j(0)\,|\,u_j(\delta k)\rangle ... \langle u_j(\pi-2\delta k)\,|\,u_j(\pi-\delta k)\rangle \langle u_j(\pi-\delta k)\,|\,u_j(\pi)\rangle = \\ = &\langle u_j(\pi)|\,\hat{\Pi}_{\pi-\delta k}\,|u_j(\pi-\delta k)\rangle \langle u_j(\pi-\delta k)|\,\hat{\Pi}^{\dagger}_{\pi-\delta k}\hat{\Pi}_{\pi-2\delta k}\,|u_j(\pi-2\delta k)\rangle ... \\ &... \langle u_j(\delta k)|\,\hat{\Pi}^{\dagger}_{\delta k}\,|u_j(0)\rangle \langle u_j(0)\,|\,u_j(\delta k)\rangle ... \langle u_j(\pi-2\delta k)\,|\,u_j(\pi-\delta k)\rangle \langle u_j(\pi-\delta k)\,|\,u_j(\pi)\rangle, \end{aligned} \tag{2.14}$$

where the following terms can be expanded as

i) $\langle u_j(k-\delta k)\,|\,u_j(k)\rangle \simeq 1 + i\theta_k$ for $k = \delta k, 2\delta k, ..., \pi$ (2.15)

ii) $\langle u_j(k)|\,\hat{\Pi}^{\dagger}_{k}\hat{\Pi}_{k-\delta k}\,|u_j(k-\delta k)\rangle \simeq \langle u_j(k)\,|\,u_j(k-\delta k)\rangle +$

$$\langle u_j(k)| \begin{bmatrix} -i\delta k & 0 & 0 & 0 \\ 0 & 0 & 0 & 0 \\ 0 & 0 & 0 & 0 \\ 0 & 0 & 0 & 0 \end{bmatrix} |u_j(k-\delta k)\rangle \simeq 1 - i\theta_k - i\delta k \langle u_j(k,1)\,|\,u_j(k-\delta k,1)\rangle$$

for $k = \pi - \delta k, \pi - 2\delta k, ..., 2\delta k$ (2.16)

iii) $\langle u_j(\pi)|\,\hat{\Pi}_{\pi-\delta k}\,|u_j(\pi-\delta k)\rangle \simeq \langle u_j(\pi)| \begin{bmatrix} -1+i\delta k & 0 & 0 & 0 \\ 0 & 0 & 0 & 1 \\ 0 & 0 & 1 & 0 \\ 0 & 1 & 0 & 0 \end{bmatrix} |u_j(\pi-\delta k)\rangle$

$$\simeq \langle u_j(\pi)|\,\hat{\Pi}\,|u_j(\pi-\delta k)\rangle = p^{\dagger}_{\pi} \langle u_j(\pi)\,|\,u_j(\pi-\delta k)\rangle \tag{2.17}$$

vi) $\langle u_j(\delta k)|\,\hat{\Pi}_{\delta k}\,|u_j(0)\rangle \simeq \langle u_j(\delta k)| \begin{bmatrix} 1 & 0 & 0 & 0 \\ 0 & 0 & 0 & 1 \\ 0 & 0 & 1 & 0 \\ 0 & 1 & 0 & 0 \end{bmatrix} + i\delta k \begin{bmatrix} 1 & 0 & 0 & 0 \\ 0 & 0 & 0 & 0 \\ 0 & 0 & 0 & 0 \\ 0 & 0 & 0 & 0 \end{bmatrix} |u_j(0)\rangle \simeq$

$$\simeq \langle u_j(\delta k)|\,\hat{\Pi}\,|u_j(0)\rangle = p_0 \langle u_j(\delta k)\,|\,u_j(0)\rangle \tag{2.18}$$

Notice that, since we require that $\delta k \to 0$, the terms with this dependence in **iii)** and **vi)** were disregarded as an infinitesimal surface term and the inversion matrix becomes k-independent. The Wilson loop can then be written as the following

$$\mathcal{W}_j = p_\pi^\dagger \langle u_j(\pi) \,|\, u_j(\pi - \delta k)\rangle \langle u_j(\pi - \delta k) \,|\, u_j(\pi)\rangle \, p_0 \, \langle u_j(\delta k) \,|\, u_j(0)\rangle \langle u_j(0) \,|\, u_j(\delta k)\rangle$$

$$\prod_{k=2\delta k}^{\pi-\delta k} \langle u_j(k-\delta k) \,|\, u_j(k)\rangle \langle u_j(-k) \,|\, u_j(-k+\delta k)\rangle = p_\pi^\dagger p_0 \prod_{k=2\delta k}^{\pi-\delta k} (1 - i\delta k \, \langle u_j(k,1) \,|\, u_j(k-\delta k,1)\rangle). \tag{2.19}$$

With this result we can simply deduce the Zak's phase using

$$\mathcal{Z}_j = \arg\left(\lim_{\delta k \to 0} \mathcal{W}_j\right) = \arg\left(p_\pi^\dagger p_0\right) - \int_0^\pi dk |u_j(k,1)|^2 \tag{2.20}$$

since $\langle u_j(k,1) \,|\, u_j(k-\delta k,1)\rangle \approx |u_j(k,1)|^2$ for $\delta k \to 0$.

The above expression is equivalent to the previous Zak's phase plus a correction due to the non-centralized inversion symmetry of the above system mentioned. This correction implies that the results of this topological invariant is no longer quantized.

In order to obtain the general correction for any given lattice, we have to take into account the position of the inversion centre with respect to the unit cell. If, for instance, the number N of sites in the unit cell of an one-dimensional chain is an odd number, the centre of the unit cell corresponds to a site and is located in between two sites if N is even. Let us consider the site position $r_j = a(j - 1/2)/N$ for $j = 1, ..., N$ and the position of the inversion centre $r_c = a(1/2 + m/2N)$ for $m = 0, \pm 1, ..., \pm N$ where a is the length of the unit cell, a/N is the separation between consecutive sites, j is the labelled number of each site and m the displacement of the inversion centre with respect to the midpoint of the unit cell. For this configuration, if $m = 0$ the centre of the unit cell is equal to the middle point of the unit cell and the inversion operator corresponds to a matrix of ones in the antidiagonal (with one element coincident with the main diagonal if N is odd). Since $\hat{\Pi}$ is independent of k, the correction does not apply in this case. On the other hand, if $m < 0$ ($m > 0$) there is a displacement to the left (right) with respect to the midpoint of the unit cell and the inversion operator is written as

$$\begin{cases} \hat{\Pi}_k = \begin{bmatrix} M1_{|m|} & \mathbf{0} \\ \mathbf{0} & M2_{|m|} \end{bmatrix} & \text{for } r_c < \dfrac{a}{2} \\ \\ \hat{\Pi}_k = \begin{bmatrix} M2^\dagger_{|m|} & \mathbf{0} \\ \mathbf{0} & M1_{|m|} \end{bmatrix} & \text{for } r_c > \dfrac{a}{2} \end{cases} \tag{2.21}$$

where M1 is a matrix $(N - |m|) \times (N - |m|)$ of ones in the antidiagonal and M2 is a $|m| \times |m|$ matrix with elements e^{-ik} in the antidiagonal as follows

$$M1_{|m|} = \begin{bmatrix} 0 & 0 & 0 & 1 \\ 0 & 0 & \iddots & 0 \\ 0 & \iddots & 0 & 0 \\ 1 & 0 & 0 & 0 \end{bmatrix}, \quad M2_{|m|} = \begin{bmatrix} 0 & 0 & 0 & e^{-ik} \\ 0 & 0 & \iddots & 0 \\ 0 & \iddots & 0 & 0 \\ e^{-ik} & 0 & 0 & 0 \end{bmatrix}. \tag{2.22}$$

The general formula for the corrected Zak's phase is written taking into account the number of terms in $\hat{\Pi}_k$ that have dependence on k, that is

$$\mathcal{Z}_j = \arg\left(p_0 p_\pi^\dagger\right) \mp \sum_{|m|} \int_0^\pi dk |u_j(k, |m|)|^2. \tag{2.23}$$

2.2 Chiral Symmetry

Frequently, a system is said to have chiral symmetry whenever a transformation over the Hamiltonian results in

$$\hat{\mathcal{C}}\hat{H}\hat{\mathcal{C}}^{\dagger} = -\hat{H}. \tag{2.24}$$

With this, the chiral operator $\hat{\mathcal{C}}$ must be Hermitian, $\hat{\mathcal{C}}^{\dagger} = \hat{\mathcal{C}}$, and obey the condition $\hat{\mathcal{C}}^2 = \hat{\mathcal{C}}^{\dagger}\hat{\mathcal{C}} = 1$. Nonetheless, the chiral operator may acquire a state-independent phase $\hat{\mathcal{C}}^2 = e^{i\phi}$ which can be suppressed by redefinition of $\hat{\mathcal{C}}$.

Other requirements for this particular symmetry operator may also be mentioned. For instance, $\hat{\mathcal{C}}$ must be local, meaning it acts on the unit cell rather than the global system. This statement implies that matrix elements of $\hat{\mathcal{C}}$ between sites of different unit cells should vanish $\langle j, \alpha | \hat{\mathcal{C}} | l, \alpha' \rangle = 0$. We can then decompose the global chiral operator into local operators acting on the internal Hilbert space of the unit cell as

$$\hat{\mathcal{C}} = \bigoplus_{j=1}^{N_{cell}} \hat{\mathcal{C}}_j. \tag{2.25}$$

Another requirement is the robustness of the chiral operator to certain disorders applied to the system. This means that $\hat{\mathcal{C}}$ will remain independent to variations in local parameters of the Hamiltonian [16].

The chiral symmetry relates two non-degenerate eigenstates of the Hamiltonian with symmetric energy values such that, if $\hat{H}|\psi\rangle = \epsilon|\psi\rangle$ then there is chiral pair $\hat{\mathcal{C}}|\psi\rangle$ which obeys $\hat{H}\hat{\mathcal{C}}|\psi\rangle = -\epsilon\ \hat{\mathcal{C}}|\psi\rangle$. From this last relation we take the anticomutation property $\{\hat{H}, \hat{\mathcal{C}}\} = 0$. Consider a bipartite system with two sites $\{\alpha, \beta\}$ per unit cell so that the chiral operator is defined using the sublattice projectors as $\hat{\mathcal{C}} = \hat{P}_{\alpha} - \hat{P}_{\beta}$. Since the chiral pairs have different energies and assuming $\epsilon \neq 0$ they must be orthogonal to each other implying that the amplitudes will be equally divided between the two sublattices,

$$\langle\psi|\left(\hat{\mathcal{C}}|\psi\rangle\right) = 0 \Rightarrow \langle\psi|\hat{P}_{\alpha}|\psi\rangle = \langle\psi|\hat{P}_{\beta}|\psi\rangle. \tag{2.26}$$

Moreover, to find the chiral pair of $|\psi\rangle$ in this system, one may simply flip the sign of the wavefunction in sublattice-β, since the chiral operator does not mix amplitudes between different sites. In the case where $\epsilon = 0$, the zero energy state is its own chiral symmetric partner and must be an eigenstate of $\hat{\mathcal{C}}$, which implies that the wavefunction has support in only one sublattice [30].

2.2.1 Application to the Su-Schrieffer-Heeger model

In this chapter, we make use of the Su-Schrieffer-Heeger (SSH) model to study the concepts of inversion and chiral symmetry, topological invariants and protected edge states in order to generalize for the Lieb lattice. The SSH model is a one-dimensional lattice with staggered hopping probabilities used to describe the behaviour of single spinless fermions [16, 8, 31]. It is well-known that the SSH model with OBC and integer number of diatomic unit cells exhibits two topologically distinct phases followed by a gap opening in which only one of these acquires two zero energy localized edge states due to the dimerization of the lattice. Because of its geometric simplicity, this particular model is used to study the properties of topological insulators, more precisely, the transition between distinct topological phases and its implications.

2.2.1.1 Band structure of the periodic model

The SSH chain consists of a one dimensional lattice with two sites per unit cell $\{A, B\}$, staggered nearest neighbour hopping amplitudes $\{t_1, t_2\}$ and correspondent tight-binding Hamiltonian in the Wannier basis[1]

$$H = -\sum_j \left(t_1 c_{j,A}^\dagger c_{j,B} + t_2 c_{j,B}^\dagger c_{j+1,A} + H.c. \right) \tag{2.27}$$

where $\{c_{j,A}^\dagger, c_{j,B}^\dagger\}$ are the creation operators in site A and B of unit cell j, respectively. Considering periodic boundary conditions (PBC) and translation invariance of the bulk we apply a Fourier transform using the Bloch's wavefunctions such that $c_{k,M} = \frac{1}{\sqrt{N}} \sum_j e^{ikj} c_{j,M}$ with $M = \{A, B\}$. The bulk momentum-space matrix Hamiltonian in the new basis reads

$$H(k) = \begin{bmatrix} 0 & \rho^*(k) \\ \rho(k) & 0 \end{bmatrix} \tag{2.28}$$

with $\rho(k) = |\rho(k)|e^{i\theta_k} = t_1 + t_2 e^{ik}$. The exponential factor that comes multiplied by t_2 reflects the fact that, in concordance with the Bloch's theorem, this is an intercell hopping amplitude connecting two sites from adjacent unit cells. The energy bands are obtained calculating the eigenvalues of $H(k)$, which gives

$$\epsilon_{k,\pm} = \pm|\rho(k)| = \pm\sqrt{2t_1 t_2 \cos k + t_1^2 + t_2^2} \tag{2.29}$$

and the correspondent eigenvectors are $|\psi_{k,\pm}\rangle = |k\rangle \otimes |u_{k,\pm}\rangle$ with

$$|u_{k,\pm}\rangle = \frac{1}{\sqrt{2}} \begin{pmatrix} \pm\frac{\rho^*(k)}{|\rho(k)|} \\ 1 \end{pmatrix} = \frac{1}{\sqrt{2}} \begin{pmatrix} \pm e^{-i\theta_k} \\ 1 \end{pmatrix} = \frac{1}{\sqrt{2}} \begin{pmatrix} \pm\frac{t_1 + t_2 e^{-ik}}{\sqrt{2t_1 t_2 \cos k + t_1^2 + t_2^2}} \\ 1 \end{pmatrix}. \tag{2.30}$$

We see that the first component of both eigenvectors is not fully defined due to the existence of poles, that are the solutions to the equation

$$t = -\cos k \pm \sqrt{\cos^2 k - 1} \tag{2.31}$$

where $t = t_1/t_2$. In the Argand plane, Eq.2.31 translates into two semi-circumferences from $[0, \pi]$ and $[0, -\pi]$ both with unitary radius. Since it is considered that the hopping amplitude takes real values, the intersection between these two curves and the real axis takes place at $t = 1$ for $k = [-\pi, \pi]$ and $t = -1$ for $k = 0$. Considering the case $\{t_1, t_2\} > 0$, the transition point is then defined as $t_1 = t_2 = 1$.

According to Fig.2.3, which illustrates the behaviour of the first component of $|u_{k,+}\rangle$ as a function of both k and t, we note that the wavefunction phase ranges from $[-\pi, \pi]$ for all values of $t < 1$, reflecting an unitary winding number in this regime. In this regime, the phase extremes of $|u_{k,+}, 1\rangle$ are given by $k = \{-\pi, \pi\}$. When we reach the transition point, however, the wavefunction argument acquires values inferior to $|\pi/2|$. Moreover, for this regime, the phase range of $|u_{k,+}, 1\rangle$ depends on t and decreases the further t_1 exceeds t_2. Fig.2.3 allow us to identify the π-state as the responsible for the topological transition since $|u_{\pi,+}, 1\rangle$ curve is not smooth over the t scanning around point $t = 1$. In fact, the k-space Hamiltonian for $k = \pi$ is given by $H(k = \pi) = (t_1 - t_2)\hat{\sigma}_x$ and the respective eigenvectors are

$$|u_{\pi,\pm}\rangle = \frac{1}{\sqrt{2}} \begin{pmatrix} \pm\frac{t_1 - t_2}{|t_1 - t_2|} \\ 1 \end{pmatrix}. \tag{2.32}$$

[1] Even though second quantization is used, this system can simply be described by a single-particle Hamiltonian since we neglect interactions between electrons.

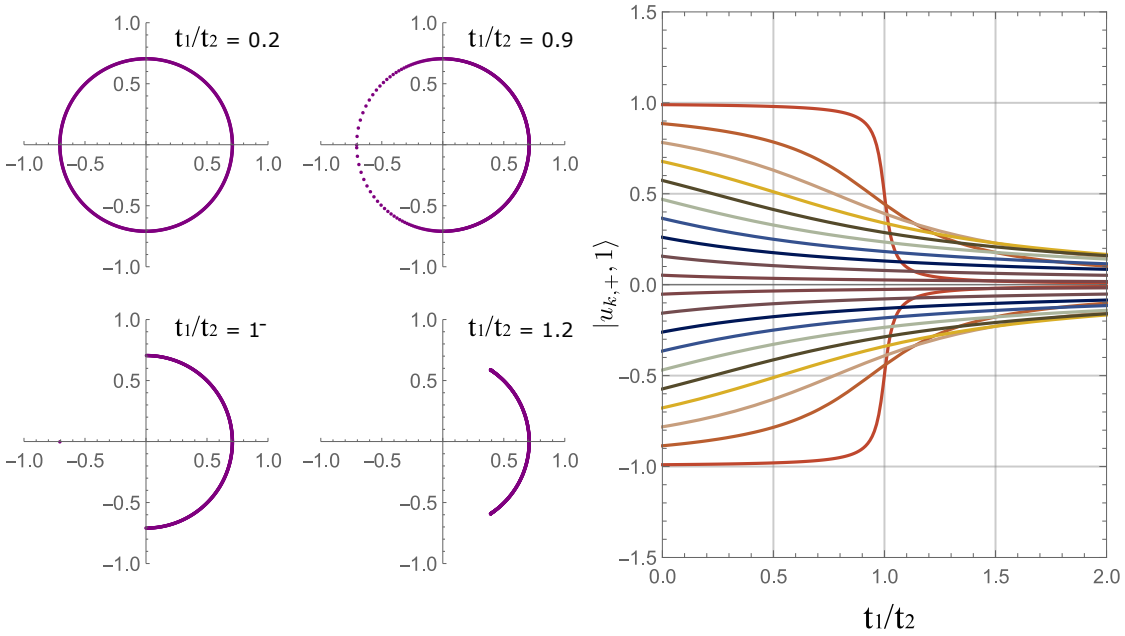

Figure 2.3: Evaluation of $|u_{k,+}\rangle$ as a function of momentum and hopping terms for the SSH chain. Left - Plots of the first component, $|u_{k,+}, 1\rangle$, for different $t_1/t_2 = \{0.2, 0.9, 1^-, 1.2\}$ and $k = [-\pi, \pi]$; Right - Behaviour of $|u_{k,+}, 1\rangle$ as a function of t_1/t_2 for several values of $k =]-\pi, \pi[$. The outmost curves in red are $k \simeq \pm\pi$ states.

The first component of these states remains constant except when we reach $t_1 = t_2$. At this point, the sign changes and the overall parity value is modified. For instance, in case of $|u_{\pi,+}\rangle$ the state changes from odd to even parity symmetry for increasing values of t.

2.2.1.2 Appearance of edge states

The last result for the parity modification on the eigenbasis of the Hamiltonian (more specifically, for states $k = \{0, \pi\}$) will induce a variation on the total Zak's phase for this system, which suggests the existence of edge states when considering OBC.

Moreover, the type of OBC will constrain the existence and number of localized boundary states. For an one-dimensional chain with N sites, applying open conditions is equivalent to add virtual sites in both terminations where the wavefunction amplitude is zero. Given the Wannier states $|j, \alpha\rangle$ and $|j, \gamma\rangle$ of the first, α, and last, γ, sites of unit cell j we must create a virtual site $|0, \gamma\rangle$ in the beginning and a $|N+1, \alpha\rangle$ in the end of the chain. Ultimately, to find the eigenstates for the finite system, we shall divide them into two categories: harmonic-like and edge states. The former are linear combinations of k-space eigenstates of the infinite chain $|k\rangle \otimes |u_k\rangle$ and $|k\rangle \otimes |u_{-k}\rangle$ which will generate nodes at the virtual sites[2] either by anti-bonding combination or by the choice of momentum k [33]. For the edge state, we will have a localized wavefunction in one boundary along with a zero amplitude in a sublattice, assuring the implementation of OBC.

In the SSH system, if both terminations of the chain are t_1 or t_2 hoppings, we will have an integer number of unit cells and two edge states localized in opposite endings of the chain, with non-zero energy, emerging for one of the dimerization limits. For this case, the system reveals inversion symmetry (with inversion centre localized in the middle of the chain) and

[2] An eigenstate of the infinite chain with two nodes in sites $\{\alpha, \beta\}$ will remain an eigenstate of the finite chain attained breaking the infinite chain in sites $\{\alpha, \beta\}$ [32].

the edge states are chiral pairs with symmetric energies.

Otherwise, the model will display a single zero energy edge state localized in one of the two ends of the chain, depending on t. This edge state is its own chiral pair and must be an eigenstate of the chiral operator for the SSH model such that

$$\hat{\mathcal{C}} \left|\text{edge}\right\rangle = \mathsf{c} \left|\text{edge}\right\rangle \tag{2.33}$$

with

$$\hat{\mathcal{C}} = \sigma_z = \begin{bmatrix} 1 & 0 \\ 0 & -1 \end{bmatrix} \tag{2.34}$$

and correspondent eigenvectors $\{(1,0),(0,1)\}$ and eigenvalues $\mathsf{c} = \pm 1$. To satisfy Eq.2.33, the state may not acquire finite energy near the topological transition point and one of the sublattices must have zero amplitude, once the chain is bipartite. Assuming the amplitude of the edge state has an exponential behaviour of the form c^j, being maximum in the boundary where is found localized and decaying in the direction of the bulk, we may obtain the analytical form of edge-like[3] states using the tight-binding equations for the wavefunction amplitudes in the infinite chain and applying the required open boundary conditions. We may look for states in the basis $\{\left|A_j\right\rangle, \left|B_j\right\rangle\}$ of the form

$$\left|u_j\right\rangle = c^j \begin{pmatrix} \psi_A \\ \psi_B \end{pmatrix}. \tag{2.35}$$

which, according to Eq.2.27, are solutions of the tight-binding equations

$$\begin{cases} \epsilon c^j \psi_A = t_1 \psi_B c^j + t_2 \psi_B c^{j-1} \\ \epsilon c^j \psi_B = t_1 \psi_A c^j + t_2 \psi_A c^{j+1} \end{cases} \tag{2.36}$$

or, equivalently

$$\epsilon \begin{bmatrix} \psi_A \\ \psi_B \end{bmatrix} = \begin{bmatrix} 0 & t_1 + t_2 c^{-1} \\ t_1 + t_2 c & 0 \end{bmatrix} \begin{bmatrix} \psi_A \\ \psi_B \end{bmatrix}. \tag{2.37}$$

From this system, we obtain the energy eigenvalues as $\epsilon_\pm = \pm\sqrt{(t+1/c)(t+c)}$ where we impose that $\{-t, -1/t\} < c < \{-1/t, -t\}$ to assure real values of ϵ. The respective eigenstates can be written as

$$\begin{bmatrix} \psi_A \\ \psi_B \end{bmatrix} = \begin{bmatrix} \pm\sqrt{t+1/c} \\ \sqrt{t+c} \end{bmatrix}. \tag{2.38}$$

Eq.2.38 reproduces the form of edge-like states for an infinite chain. For the state to be an eigenstate of the finite chain, we may impose OBC, i.e., establish the sublattice which contains the virtual site and set the correspondent amplitudes to zero. Recall that we are analysing the situation where the terminations of the chain are t_1 and t_2 hoppings causing the virtual sites to belong to the same sublattice. Thus, if we constrain $\psi_B = 0$ independently of unit cell j then sublattice-A is ruled by an exponential function with decaying constant $c = -t$ and the dependence on the hopping amplitudes results in a left (right) edge state when $t < 1$ ($t > 1$). If we set $\psi_A = 0$, then we have $c = -1/t$ which will become a right (left) edge state when $t < 1$ ($t > 1$). At the symmetric point $t_1 = t_2$ both edge-states turn into a standing wave with $k = \pi/2$. Note that, from this solution, the OBC is guaranteed without the possibility of finite size effects.

[3]Some states may have an amplitude distribution of c^j form with $c \to -1$. These eigenfunctions may be solutions of the tight-binding equations, however, they are not edge states in the sense that the level of localization in the terminations of the chain is not significant.

2.2.1.3 Perturbations to the SSH model

Consider an open SSH chain with N sites. Using Eq.2.25 and knowing the chiral operator for this system follows Eq.2.34, we may write the chiral transformation over a generic matrix M with elements a_{ij} (representation of an operator in the Wannier basis) as

$$\hat{\mathcal{C}}M\hat{\mathcal{C}}^{\dagger} = \begin{bmatrix} 1 & 0 & 0 & 0 & \cdots \\ 0 & -1 & 0 & 0 & \cdots \\ 0 & 0 & 1 & 0 & \cdots \\ 0 & 0 & 0 & -1 & \cdots \\ \vdots & \vdots & \vdots & \vdots & \ddots \end{bmatrix} . \begin{bmatrix} a_{11} & a_{12} & a_{13} & a_{14} & \cdots \\ a_{21} & a_{22} & a_{23} & a_{24} & \cdots \\ a_{31} & a_{32} & a_{33} & a_{34} & \cdots \\ a_{41} & a_{42} & a_{43} & a_{44} & \cdots \\ \vdots & \vdots & \vdots & \vdots & \ddots \end{bmatrix} . \begin{bmatrix} 1 & 0 & 0 & 0 & \cdots \\ 0 & -1 & 0 & 0 & \cdots \\ 0 & 0 & 1 & 0 & \cdots \\ 0 & 0 & 0 & -1 & \cdots \\ \vdots & \vdots & \vdots & \vdots & \ddots \end{bmatrix} =$$

$$= \begin{bmatrix} a_{11} & -a_{12} & a_{13} & -a_{14} & \cdots \\ -a_{21} & a_{22} & -a_{23} & a_{24} & \cdots \\ a_{31} & -a_{32} & a_{33} & -a_{34} & \cdots \\ -a_{41} & a_{42} & -a_{43} & a_{44} & \cdots \\ \vdots & \vdots & \vdots & \vdots & \ddots \end{bmatrix} \quad (2.39)$$

We see that the SSH chiral operator will flip the sign of all elements where the sum $i + j$ is odd. Assuming this generic matrix M is now the Hamiltonian of the system we conclude that, if the elements where $(i + j) \mod 2 = 0$ are not equal to zero we will not satisfy the chiral property $\hat{\mathcal{C}}H\hat{\mathcal{C}}^{\dagger} = -H$. A consequence of this chiral property, stated in Section 2.2, is the anticommutation relation between $\hat{\mathcal{C}}$ and H. We have seen that the edge state must be an eigenstate of both H and $\hat{\mathcal{C}}$ and that will automatically imply that the energy for this state vanishes since

$$\{\hat{\mathcal{C}}, H\} \left|edge\right\rangle = 0 \left|edge\right\rangle \Rightarrow \hat{\mathcal{C}}H \left|edge\right\rangle = -H\hat{\mathcal{C}} \left|edge\right\rangle$$
$$\Rightarrow \pm\epsilon \left|edge\right\rangle = \mp\epsilon \left|edge\right\rangle \Rightarrow \epsilon = 0. \quad (2.40)$$

Let us examine a simple example of a t_1t_2-SSH chain with three sites and real space Hamiltonian and chiral operator given by

$$H = \begin{bmatrix} \alpha_{11} & t_1 & \beta_{13} \\ t_1 & \alpha_{22} & t_2 \\ \beta_{31} & t_2 & \alpha_{33} \end{bmatrix} \quad , \quad \hat{\mathcal{C}} = \begin{bmatrix} 1 & 0 & 0 \\ 0 & -1 & 0 \\ 0 & 0 & 1 \end{bmatrix} . \quad (2.41)$$

In the unperturbed system, we have $\{\alpha_{ij}, \beta_{kl}\} = 0$ and the chiral property is preserved. The correspondent eigensystem of H follows

$$\epsilon_1 = 0; \qquad \left|\psi_1\right\rangle = \begin{pmatrix} -t_2/t_1 \\ 0 \\ 1 \end{pmatrix}; \quad (2.42)$$

$$\epsilon_2 = -\sqrt{t_1^2 + t_2^2}; \qquad \left|\psi_2\right\rangle = \begin{pmatrix} t_1/t_2 \\ -\dfrac{\sqrt{t_1^2 + t_2^2}}{t_2} \\ 1 \end{pmatrix}; \quad (2.43)$$

$$\epsilon_3 = \sqrt{t_1^2 + t_2^2}; \qquad \left|\psi_3\right\rangle = \begin{pmatrix} t_1/t_2 \\ \dfrac{\sqrt{t_1^2 + t_2^2}}{t_2} \\ 1 \end{pmatrix}; \quad (2.44)$$

where the eigenvectors need normalization. The first state is an eigenstate of the chiral operator and corresponds to a zero energy edge state, thus satisfying Eq.2.40. The localization of this edge state in the open chain will depend on the hopping amplitudes as we can observe from the first component of the eigenvector $|\psi_1\rangle$, being a left (right) edge state for $t_2/t_1 < 1$ ($t_2/t_1 > 1$). The transition point occurs when the components of the edge state are unitary (the distribution behaviour evolves from exponentially localized to standing wave) so we recover $t_1 = t_2$. Looking at the last two states, we may conclude they are chiral pairs since they have symmetric energy values and the amplitude of the wavefunction is equally divided between the two sublattices (Eq.2.26).

Allowing one of the elements $\{\alpha_{ij}, \beta_{kl}\}$ of the Hamiltonian (which translates as onsite potentials and next nearest neighbour hoppings, respectively) to be finite will break the chiral property which recognizes a system as chiral symmetric, according to Eq.2.39. For instance, if we include a staggered potential such that different sublattices will have symmetric onsite energies, the correspondent Hamiltonian and eigensystem read

$$\epsilon_1 = \alpha; \qquad |\psi_1\rangle = \begin{pmatrix} -t_2/t_1 \\ 0 \\ 1 \end{pmatrix}; \tag{2.45}$$

$$H = \begin{bmatrix} \alpha & t_1 & 0 \\ t_1 & -\alpha & t_2 \\ 0 & t_2 & \alpha \end{bmatrix}, \quad \epsilon_2 = -\sqrt{\alpha^2 + t_1^2 + t_2^2}; \quad |\psi_2\rangle = \begin{pmatrix} t_1/t_2 \\ \dfrac{-\alpha - \sqrt{\alpha^2 + t_1^2 + t_2^2}}{t_2} \\ 1 \end{pmatrix}; \tag{2.46}$$

$$\epsilon_3 = \sqrt{\alpha^2 + t_1^2 + t_2^2}; \qquad |\psi_3\rangle = \begin{pmatrix} t_1/t_2 \\ \dfrac{-\alpha + \sqrt{\alpha^2 + t_1^2 + t_2^2}}{t_2} \\ 1 \end{pmatrix}; \tag{2.47}$$

In this case, the edge state is no longer a zero energy eigenstate thus breaking the chiral property of Eq.2.40. Nevertheless, since the eigenvector remains identical to the unperturbed system, we still have an edge state whose direction of localization depends on the hopping amplitudes and the same transition point. In what concerns the two last states, their energy remain symmetric although they are no more chiral pairs in the sense that $\hat{\mathcal{C}}\,|\psi_2\rangle \neq |\psi_3\rangle$ and their wavefunction amplitude is not equally shared between the two sublattices. These two last conditions will only be fulfilled when we approach $\alpha \to 0$.

We may state that, even though we lost the chiral property for this system, we still observe that the edge state remains protected from the energy splitting of states $\{|\psi_2\rangle, |\psi_3\rangle\}$ (note that, as α grows the edge state approaches level ϵ_3 but remains in the middle of the two levels).

2.2.2 Generalization of the chiral operator

We saw in the SSH model that, for certain OBC imposed, we may obtain a zero energy edge state which is protected[4] by chiral symmetry, meaning it satisfies Eq.2.33. For other more complex models (in terms of dimensionality, symmetry and number of sites and next-neighbour hoppings per unit cell) and for particular choices of OBC, these protected edge states often appear isolated between two bands and have finite energies. Furthermore, the application of a local potential to the Hamiltonian may break the chiral symmetry rule of

[4]The fact that it is a protected state means it will remain an edge state for certain perturbations such as variations in the local parameters of the Hamiltonian. In the SSH model, these parameters are often the hopping amplitudes $\{t_1, t_2\}$.

Eq.2.24, however, we still may not lose the protection associated with these states. Hence, a generalization may be done if we ought to define a chiral operator which predicts the existence of topological protected edge states for any given system. The following conditions were established using the properties observed in the SSH model and inferring for systems which behaviour we acknowledge:

- The operator $\hat{\mathcal{C}}$ must pair non-degenerate eigenstates in a given subset of the eigenbasis of the Hamiltonian. This means that, for an eigenstate $|\psi_1\rangle$ with energy ϵ_1, we can find the correspondent "chiral" pair $|\psi_2\rangle = \hat{\mathcal{C}}\,|\psi_1\rangle$ with energy ϵ_2 in a subset of all the eigenstates of H where $\hat{\mathcal{C}}^2 = 1$ holds. Exceptionally, when $\epsilon_1 = \epsilon_2$ the pairing operation should state that $\hat{\mathcal{C}}\,|\psi\rangle = \mathsf{c}\,|\psi\rangle$ and $|\psi\rangle$ is an eigenstate of H and $\hat{\mathcal{C}}$.
- The system in which we define $\hat{\mathcal{C}}$ should have dimerized limits where edge states appear at one end of the chain depending on the OBC provided.
- At the symmetry point, $\hat{\mathcal{C}}$ acts on the eigenstates of the bulk Hamiltonian as a momentum shift operator.
- We may energetically split the system into subsets where the pair operation will act. This subset shall contain the chiral pair band of all k-states and a single edge state. With this, we aim to break up more complex systems into several SSH-like models and apply the same formulation for each subset.
- For the infinite system and in the chiral pair basis $\{|\psi_{k,1}\rangle, |\psi_{k,1p}\rangle, ..., |\psi_{k,n}\rangle, |\psi_{k,np}\rangle\}$ with n the number of chiral pairs, the chiral operator must satisfy $\hat{\mathcal{C}}(k)\,|\psi_{k,j/jp}\rangle = |\psi_{k,jp/j}\rangle$ and $\hat{\mathcal{C}}^{\dagger}(k)\hat{H}(k)\hat{\mathcal{C}}(k) = \hat{H}(k; \epsilon_{k,j} \leftrightarrow \epsilon_{k,jp}), \forall j \in [1, n]$.
- Knowing how the chiral operator acts on k-subspaces we can write

$$\hat{\mathcal{C}} = \sum_k \hat{\mathcal{C}}(k) = \sum_k |\psi_{k,1}\rangle\langle\psi_{k,1p}| + \cdots + |\psi_{k,n}\rangle\langle\psi_{k,np}| + H.c. = \oplus_k \hat{\mathcal{C}}(k) \tag{2.48}$$

  where $\hat{\mathcal{C}}(k)$ is the square matrix chiral operator with dimension equal to the number, n, of sites in the unit cell of the system. Since there is no mixing between different k-subspaces, the overall matrix representation will be block-diagonal. From Eq.2.48 we take the eigenvalues of $\hat{\mathcal{C}}$ as $\mathsf{c} = \pm 1$ with degeneracy equal to the number of k-subspaces times the number of chiral pairs.
- Each k-space chiral pair gives rise to an edge state in the open system. The edge state is its own chiral pair so that we have

$$\hat{\mathcal{C}}\,|\text{edge}\rangle = \mathsf{c}\,|\text{edge}\rangle \tag{2.49}$$

  In addition, for this edge state to be an eigenstate of the open system with OBC such that γ is the chosen virtual site, we require $\langle 0, \gamma\,|\,\text{edge}\rangle = 0$.

Chapter 3
Two Dimensional Lieb Lattice

In this chapter, we treat the main characteristics of the bulk and boundaries found in the two-dimensional Lieb system. Open boundary conditions are imposed and the different localized plaquette and edge states are studied. The analysis of the different symmetries present in the lattice allowed for the proposal of a modified version of the Lieb system and the resulting boundary modes are discussed.

3.1 Band structure of the Lieb lattice

The Lieb lattice is a decorated line-centred square lattice characterized by three species of atoms (A,B,C) per unit cell. In terms of its connectivity, atoms A have four nearest neighbours while atoms of species (B, C) only have two nearest neighbours (Fig.3.1). The total size of the system is given by the number of plaquettes - squares of eight atoms - in both directions so that $N_p = N_{px}N_{py}$ and the total number of atoms is given by $N = 8+5(N_{px}+N_{py}-2)+3(N_{px}-N_{py}+1)$ for $\{N_{px}, N_{py}\} > 1$ and simply $N = 8+5(N_{px}+N_{py}-2)$ otherwise. This particular lattice is easily obtained from the simple square lattice by extracting each second atom when scanning the system both in the x and y direction, removing a quarter of the total atoms. It can also be built by introducing an atom between nearest neighbour atoms of the square lattice.

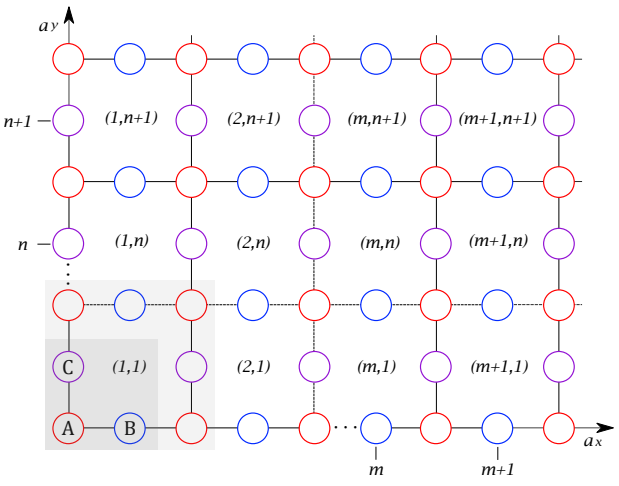

Figure 3.1: Notation of the two dimensional Lieb lattice. {A,B,C} denote the three species of sites in the unit cell and (m, n) is the plaquette label in the (x, y) direction.

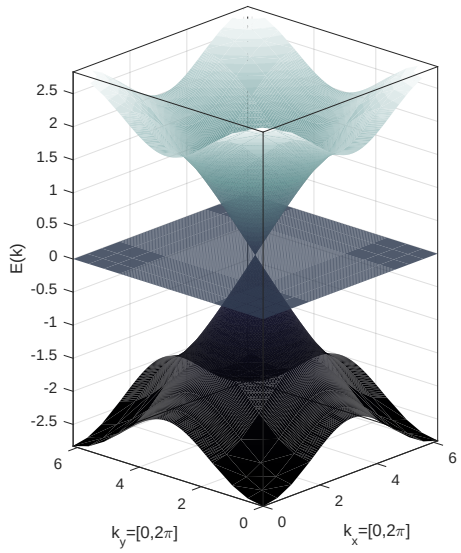

Figure 3.2: Dispersion relation of the Lieb lattice. Around point $k = [\pi, \pi]$ a Dirac cone is showcased.

In the Lieb system, electrons can hop between nearest-neighbour atoms with a certain hopping parameter t. The generic Hamiltonian for the tight-binding model of non-interacting fermions is given by

$$H = -\sum_{i,j} t_{i,j} c_i^\dagger c_j + \sum_i \epsilon_c c_i^\dagger c_i + H.c. \tag{3.1}$$

where $c_i^\dagger$ creates a fermion in site i and t_{ij} is the hopping parameter between nearest-neighbour sites i and j, neglecting the possibility of longer-range hopping [34, 35] (note that $\{i, j\}$ can represent any position in a space of arbitrary dimensions). For our particular system we specify the creation and annihilation operators acting on each of the three species of atoms (A, B, C) of cell index (m, n). Given this, the spinless Hamiltonian of the Lieb lattice in the absence of magnetic field reads

$$H_{TB} = \sum_{m,n} t\left(a^\dagger_{m,n}b_{m,n} + a^\dagger_{m,n}c_{m,n} + a^\dagger_{m,n}b_{m-1,n} + a^\dagger_{m,n}c_{m,n-1} + H.c.\right) + \\ + \epsilon_A a^\dagger_{m,n}a_{m,n} + \epsilon_B b^\dagger_{m,n}b_{m,n} + \epsilon_C c^\dagger_{m,n}c_{m,n} + H.c. \quad (3.2)$$

where we assume the hopping parameter to be constant along the system, independently of the plaquette position. The first two terms of the upper line of Eq.3.2 are intra-unit cell while the following two terms are inter-unit cell and are responsible for the connection between plaquettes. The second line gives the onsite potencials and usually dictates the symmetry of the lattice. For instance, a C_4 symmetry on the Lieb lattice implies that $\epsilon_B = \epsilon_C$ which will in turn have an effect on the band structure [35].

In order to obtain the dispersion relation of the Lieb lattice assuming periodic boundary conditions we proceed by performing the Fourier transform on the operators of Eq3.2 using

$$\begin{pmatrix} a_{k_x,k_y} \\ b_{k_x,k_y} \\ c_{k_x,k_y} \end{pmatrix} = \frac{1}{\sqrt{MN}} \sum_{m,n} \begin{pmatrix} a_{m,n} \\ b_{m,n} \\ c_{m,n} \end{pmatrix} e^{i(k_x m + k_y n)}. \quad (3.3)$$

where M and N are the number of unit cells in the (x, y) directions, respectively. The k-space Hamiltonian can be found by transforming the tight-binding Hamiltonian by

$$H_{TB} = \sum_k \left(a^\dagger_{k_x,k_y}, b^\dagger_{k_x,k_y}, c^\dagger_{k_x,k_y}\right) H_k \begin{pmatrix} a_{k_x,k_y} \\ b_{k_x,k_y} \\ c_{k_x,k_y} \end{pmatrix}. \quad (3.4)$$

For this transformation to hold, the momentum space Hamiltonian must be

$$H_k = \begin{bmatrix} \epsilon_A & t(1+e^{-ik_x}) & t(1+e^{-ik_y}) \\ t(1+e^{ik_x}) & \epsilon_B & 0 \\ t(1+e^{ik_y}) & 0 & \epsilon_C \end{bmatrix}. \quad (3.5)$$

with $k_x(k_y) = 2\pi p/M(N)$ for $p = 1, ..., M(N)$. The spectrum of H_k is the set of eigenvalues of this 3×3 matrix, giving the general expression for the dispersion relation in the following three distinct bands

$$\begin{cases} E_\pm(k_x, k_y) = \pm 2t\sqrt{\cos^2(k_x/2) + \cos^2(k_y/2)}, \\ E_0(k_x, k_y) = 0, \end{cases} \quad (3.6)$$

where we set the onsite potentials to zero. The spectrum is plotted in Fig.3.2 and we can see the electron-hole symmetry regarding the top and bottom bands. These two mirrored bands imply that, for each eigenstate in the top band with Bloch wavevector k and energy ϵ_k, there exists an eigenstate with the same momentum and symmetric energy $-\epsilon_k$. A closer look at the high symmetry point $\Gamma = (\pi, \pi)$ reveals the three bands touch each other. This touching point results from the crystalline symmetry group D_{4h} of the Lieb lattice, the absence of spin-orbit coupling and the configuration of hopping parameters $t_{nm} = t$ and onsite potentials

$\epsilon_A = \epsilon_B = \epsilon_C$ [35]. If we take the expansion of $E_\pm$ around Γ we get the equation for a Dirac cone in the low-energy region $E_\pm^2 = t^2(k_x^2 + k_y^2)$. The extreme values for the energy are $E_\pm = \pm 2\sqrt{2}t$ and are situated in points $(\{0, 2\pi\}, \{0, 2\pi\})$ of the Brillouin zone. We can also observe a flat dispersionless band with constant zero energy and degeneracy of NM. The zero energy means that the group velocity also vanishes and the corresponding states do not contribute to transport. To further understand the states who give rise to each band in the spectrum, we write the respective eigenfunctions in the k-space as a linear combination of each site contribution $|\Psi(k_x, k_y)\rangle = (\alpha a^\dagger_{k_x,k_y} + \beta b^\dagger_{k_x,k_y} + \gamma c^\dagger_{k_x,k_y})\,|0\rangle$. The coefficients can be found by solving the eigenvalues equation and the corresponding eigenfunctions read

$$\begin{cases} |\Psi_0(k_x, k_y)\rangle = \dfrac{1}{\sqrt{|\Theta_x|^2 + |\Theta_y|^2}} \left(-\Theta_y b^\dagger_{k_x,k_y} + \Theta_x c^\dagger_{k_x,k_y}\right) |0\rangle\,, \\ \\ |\Psi_\pm(k_x, k_y)\rangle = \dfrac{1}{\sqrt{2}} \left(\pm a^\dagger_{k_x,k_y} + \dfrac{\Theta_x}{\sqrt{|\Theta_x|^2 + |\Theta_y|^2}} b^\dagger_{k_x,k_y} + \dfrac{\Theta_y}{\sqrt{|\Theta_x|^2 + |\Theta_y|^2}} c^\dagger_{k_x,k_y}\right) |0\rangle\,, \end{cases} \tag{3.7}$$

with $\Theta_x = t(1 + e^{ik_x})$ and $\Theta_y = t(1 + e^{ik_y})$. The expressions in Eq.3.7 indicate that the flat band is created only by B and C type orbitals and the contribution of type-A orbitals is only seen in the upper and lower bands. This distribution for the dispersion relation of the Lieb lattice provide interesting consequences. If, for instance, one wishes to shift the flat band from $E_0 = 0$, a nonzero value of the onsite potentials of atoms B and C has to be assigned. Also, in an experience where we pretend to load electrons into the Lieb lattice, initially half of the particles would be confined in A-atoms, while the other half would go to atoms B and C, in an equal share. When reaching the flat band, further loading of the particles will only increase the number of electrons in atoms B and C, while the particle density of atoms A will remain constant. Once the flat band is completely filled we start occupying the upper band which has the same behaviour as the lower band [36, 37, 38].

3.2 Lieb lattice with OBC

Previously, we have used the periodic boundary conditions to obtain the dispersion relation of the Lieb lattice. Nevertheless, in real systems, we should impose open boundary conditions to ensure that the eigenfunctions vanish along the edges. In the Lieb lattice this means we must choose between the border atoms A, B or C in each of the four edges. For instance, if the finite lattice begins and ends with an A site in the x-direction, applying open boundary conditions along this direction requires the wavefunction to be absolute zero in the B-type virtual sites of cells $(0, n)$ and $(M + 1, n)$. Moreover, as reported in [39], the three different edge geometries of the 2D Lieb lattice (straight, bearded and asymmetric) induce differences in its dispersion relation particularly in the energy gap at the high symmetry point Γ and this energy differences will depend on the number of unit cells in the system.

3.2.1 Plaquette Localized states

States of the flat band with a well defined momentum spread over the whole lattice. Still we can perform a combination of these states to form localized eigenstates with zero energy that occupy a small region of the lattice. These flat band states are composed by contributions of B and C sites with alternating amplitude signs along a plaquette loop (Eq.3.7) and the

hoppings originating from these two sites cancel each other terms in the eigenvalue equation for sites A.

Let us consider a simple form of the Lieb system with two plaquettes and a total of 13 atoms. The tight-binding Hamiltonian can be written in first quantization as $H_{TB} = \sum_j \epsilon_j |j\rangle \langle j| + \sum_{j,l} t_{j,l} |j\rangle \langle l|$ where the first term describes the onsite potentials ϵ_j and the second term the hopping between two nearest-neighbours sites j and l. The real space eigenfunction is the combination of each component localized in site j such as $\Psi_E = \sum_j \alpha_j |j\rangle$. In order to find the eigenfunctions corresponding to $E = 0$ we need to find solutions for the eigenvalue equation

$$\epsilon_j \alpha_j + \sum_l t_{j,l}\, \alpha_l = 0, \ \forall j. \tag{3.8}$$

If we consider the onsite potentials $\epsilon_j = 0$ and a constant non-zero nearest-neighbour hopping parameter $t_{j,l} = t$, then Eq.3.8 becomes simply $\sum_{l \in \aleph_j} \alpha_l = 0$ where the summation is taken for components α_l belonging to the nearest neighbours group-$\aleph$ of each site j, giving a total of N (= 13 in this case) conditions [40]. Fig.3.3 illustrates two possible eigenstates that satisfy Eq.3.8 where the left case belongs to a localized[1] state extended throughout the lattice whereas in the right case we get the most compact localized state possible to construct, confined to a single plaquette. Assuming we want to assemble an orthogonal basis in the space of the degenerate flat band eigenfunctions we must apply the condition $\sum_j \alpha_j^p \alpha_j^q = 0$ where $\Psi^p_{E=0}$ and $\Psi^q_{E=0}$ are two degenerate states. If we consider a basis consisting of compact localized states in each plaquette of the system (through translation), we will form a basis with dimension equal to the number of plaquettes in the system however, since neighbouring one-plaquette states overlap with each other, this basis will not be orthogonal [28, 41].

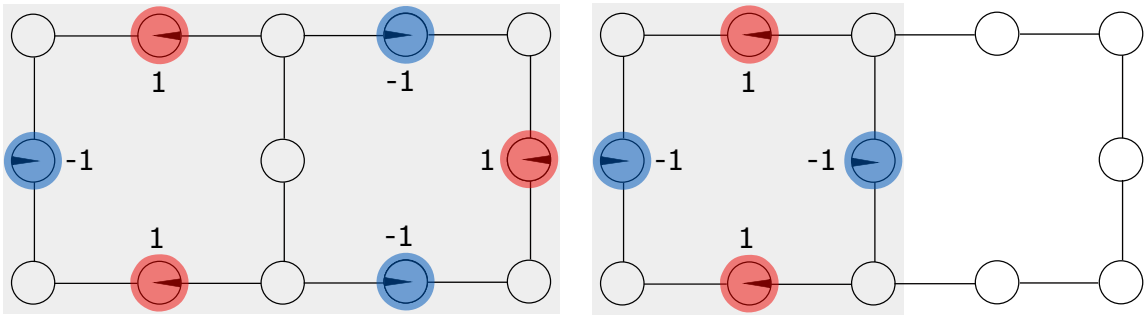

Figure 3.3: Possible localized eigenfunctions for the flat band subspace of a Lieb lattice with 13 atoms. The size of the coloured circles illustrate the amplitude probability and the colours and direction of the lines correspond to the relative differences in the phase. Left: The state is extended throughout the lattice with zero amplitudes in A and middle sites. Right: The state is confined to a single plaquette and B and C sites have opposite sign. Note that the amplitude values are not normalized.

3.2.1.1 Effect of an external magnetic field

We ought to evaluate the influence of an external magnetic field applied transversely to the lattice plane on the compact localized state. To do so, we must rewrite the tight-binding Hamiltonian of Eq.3.2 using the Peierls substitution. We know that a charged particle travelling in the presence of a magnetic field suffers a phase change of the form $\theta_l = \pi/\phi_0 \int_l^{l+1} \boldsymbol{A} \,.\, d\boldsymbol{r}$ where $\boldsymbol{A}$ is the vector potential related to the magnetic field applied as $\boldsymbol{B} = \nabla \times \boldsymbol{A}$, $\phi_0 = h/2e$ is the magnetic flux quantum and the path of integration $l \to l+1$ correspond to a hopping

[1] The term localized refers to a state that has a finite amplitude in a small region of the lattice.

between two connected sites. In the Lieb lattice there are loops in each plaquette for the particle to move, so we can associate an effective magnetic field ϕ in every single plaquette and distribute it among the 8 hopping terms using the Peierls substitution $t \to te^{i\theta_l}$ [42], so that the tight-binding Hamiltonian becomes

$$H_{TB} = \sum_{m,n} t\left(e^{i\phi y/8}a^\dagger_{m,n}b_{m,n} + e^{-i\phi x/8}a^\dagger_{m,n}c_{m,n} + e^{-i\phi y/8}a^\dagger_{m,n}b_{m-1,n} + e^{i\phi x/8}a^\dagger_{m,n}c_{m,n-1}\right) + \\ + \epsilon_A a^\dagger_{m,n}a_{m,n} + \epsilon_B b^\dagger_{m,n}b_{m,n} + \epsilon_C c^\dagger_{m,n}c_{m,n} + H.c. \quad (3.9)$$

where we have chosen the vector potential to be $\boldsymbol{A} = (-yB/2, xB/2, 0)$ and the normalized magnetic flux is $\phi = 4\pi B/\phi_0$ [43]. Fig.3.4 plots the dependence of the energy spectrum with the magnetic flux. We notice the presence of a double Hofstadter butterfly, which is a type of quantum fractal behaviour predictable in 2D lattices where the electron is subjected to both magnetic and periodic electrostatic Bloch-like potential [44]. Regarding the flat band we see that, despite the majority of the states being robust against the magnetic field, two levels separate from the zero band and acquire a dispersion dependence on ϕ. Thus, the degeneracy of the zero energy level is reduced by 2 in the presence of an external $\boldsymbol{B}$. The fact that the zero energy band remains flat in the presence of a magnetic field suggests the existence of localized states and the possibility to construct a compact state in this case as well.

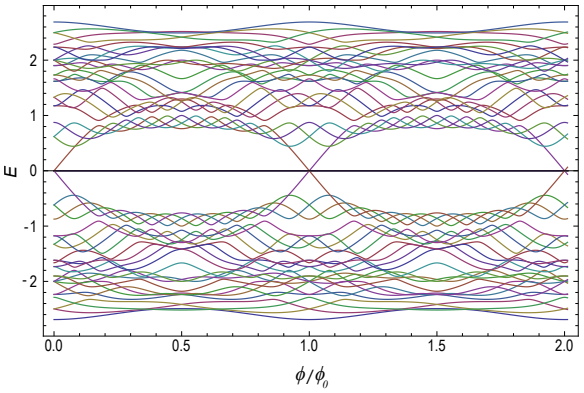

Figure 3.4: Dependence of the energy spectrum with the magnetic flux in the Lieb lattice. A double Hofstadter butterfly is seen for ϕ/ϕ_0 intervals $[0, 1]$ and $[1, 2]$.

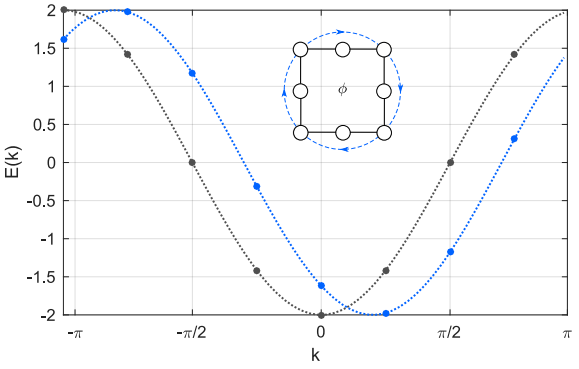

Figure 3.5: Momentum space energy for the ring system with 8 sites and $\phi = 0$ (black line) and $\phi = \pi/4$ (blue line). When a magnetic field is introduced, the symmetric k-space states are no longer degenerate.

Let us now look at the form of the previous compact localized state constructed in the absence of a magnetic field which served as a basis of the flat band (Fig.3.6a). We can distribute the plaquette flux between the eight hopping parameters accumulate the phase in only one or two hopping terms. When we run through the loop once, there is a total non-zero phase increment, so we cannot close the plaquette loop of destructive interference and the previous localized state is no longer an eigenstate of the zero energy level. Another way to look at this is by considering that one plaquette loop is analogous to a quantum ring with 8 sites and a transversal magnetic field with flux ϕ. The eigenstates of the latter system with zero flux and energies $E_k = -2t\cos(k)$ are achieved by subtracting two degenerate states $|k\rangle$ and $|-k\rangle$ to create a standing wave with zero probability density at certain sites of the ring, depending on the angular momentum. With the introduction of a magnetic field, however, the combination no longer holds (see Fig.3.5). This is because the states with opposite momenta do not have the same energy when a magnetic field is applied, since the dispersion relation is replaced by $E(k) = -2t\cos(k - \phi/N)$. Therefore, the standing wave

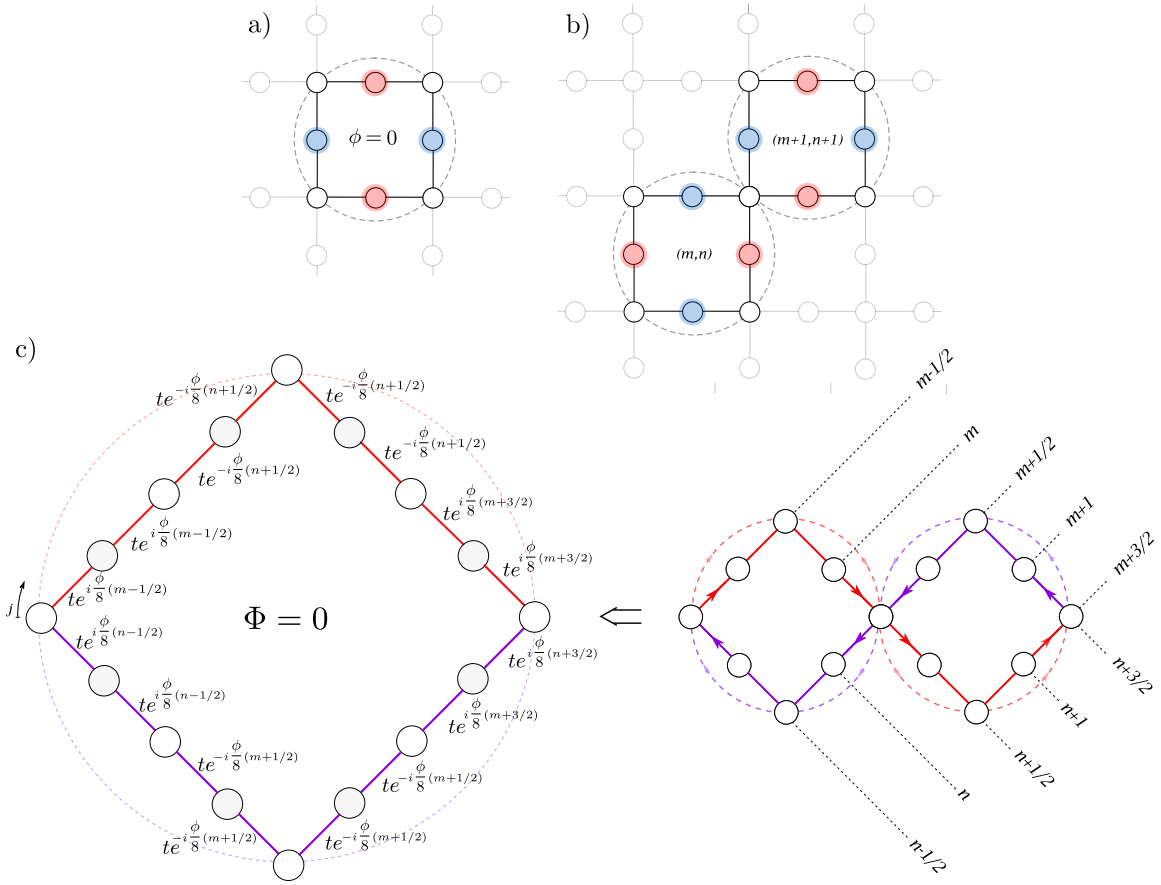

Figure 3.6: Construction of compact flat band localized states in the presence of an external magnetic field. The compact localized state (a) for $\phi = 0$ spreads to two diagonally connected plaquettes (b) in the presence of an external magnetic field, so that the total Peierls phase when following the path of the unfolded ring (c) vanishes. Sites are numbered from $j = 0$ to $j = N_R - 1$ and an even j belongs to an A-site that have zero amplitude.

---

obtained by the subtraction of these states is not an eigenstate of the system and the most compact zero energy state in the presence of flux will not be confined to a single plaquette. Instead, we need to achieve a state such that the total Peierls phase vanishes. Doing so requires following a path in two consecutive rings that share a site (where the standing wave will have a node of amplitude) so that the total phase is zero, although the phases associated with each hopping are nonzero, as suggested in Fig.3.6c. This is equivalent to considering a larger ring with total number of sites N_R equal to the two rings separated ($N_R = 16$ in the Lieb system), a standing wave with two nodes in $j = 0$ and $j = N_R/2$ created by the unfolding of the connection site of the two rings and a total flux $\Phi = 0$. The standing wave of the latter system can have more than two nodes since the number of sites is greater than 4. More precisely, since the k periodicity is given by $k = 2\pi n/N_R$ with $n = 0, 1, ..., N_R - 1$, the eigenfunctions may have a maximum of $p = N_R/2 - 1 = 7$ nodes in the Lieb lattice.

To achieve an eigenstate which is a standing wave created by the degenerate states of opposite momenta, a gauge transformation[2] has to be done so that the Peierls' phases associated with each hopping in the larger ring vanish and the translation invariance is restored.

[2]This mathematical procedure manipulates degrees of freedom of the system so that distinct configurations generate the same physical observables.

In our case and using the terminology of Eq.3.8, the gauge transformation reads

$$
\begin{aligned}
&|j\rangle \to e^{i\phi/8(m-1/2)j}\,|j\rangle\,, && j=0,...,N_R/8,\\
&|j\rangle \to e^{i\phi/8[(m-1/2)2-(n+1/2)(j-2)]}\,|j\rangle\,, && j=N_R/8+1,...,N_R/4+2,\\
&|j\rangle \to e^{i\phi/8[(m-1/2)2-(n+1/2)4+(m+3/2)(j-6)]}\,|j\rangle\,, && j=N_R/4+3,N_R/2,\\
&|j\rangle \to e^{i\phi/8[(m-1/2)2-(n+1/2)4+(m+3/2)2+(n+3/2)(j-8)]}\,|j\rangle\,, && j=N_R/2+1,N_R/2+2,\\
&|j\rangle \to e^{i\phi/8[(m-1/2)2-(n+1/2)4+(m+3/2)2+(n+3/2)2-(m+1/2)(j-10)]}\,|j\rangle\,, && j=N_R/2+3,...,N_R-2,\\
&|j\rangle \to e^{i\phi/8[(m-1/2)2-(n+1/2)4+(m^{\mathrm{a}}+3/2)2+(n+3/2)2-(m+1/2)4+(n-1/2)(N_R-j)]}\,|j\rangle\,, && j=N_R-1.
\end{aligned}
\tag{3.10}
$$

Each site j numbered clockwise in the large ring (Fig3.6c) acquires an accumulative phase. We can now construct our compact state which, in the presence of a magnetic field, extends to two plaquettes. For the state to remain localized, a zero amplitude in A-sites is imposed, leading to $\Psi_{E=0} = \sum_{j=0}^{N_R/2-1}(-1)^j\,|2j+1\rangle$. Inverting the gauge transformation, gives the final state

$$
\begin{aligned}
\Psi_{E=0} = {} & e^{i\phi/8(m-1/2)}\,|1\rangle - e^{i\phi/8(m-3/2)}\,|3\rangle + e^{-i\phi/8(m+5/2)}\,|5\rangle - e^{-i\phi/8(m+3/2)}\,|7\rangle \\
& + e^{i\phi/8(m+3/2)}\,|9\rangle - e^{i\phi/8(m+5/2)}\,|11\rangle + e^{-i\phi/8(m-3/2)}\,|13\rangle - e^{-i\phi/8(m-1/2)}\,|15\rangle\,,
\end{aligned}
\tag{3.11}
$$

which was achieved for the case $n = m$, so that the vector potential $\boldsymbol{A}$ acts on both directions equally and the symmetry is restored for these particular plaquettes (Fig.3.6b). Each localized state E_k constructed in the larger ring with the condition of nodes in $j = 0$ and $j = N_R/2$ will be associated with the flat band. However, the correspondent subspace is not only given by the translation of the localized state through other plaquettes of the lattice. In this case we have to take into account the phases associated with each site given by Eq.3.10 that arise from the increasing $\boldsymbol{A}$ in the x and y direction of the system.

3.3 Edge states in Lieb-type systems

The Lieb lattice as described through Hamiltonian in Eq.3.2 will have two types of states according to the degree of localization of the wavefunction in the system: bulk states which span through all possible k values and plaquette localized states of zero energy. For this system, in order to observe topological phase transitions with the emergence of edge states, we need to implement varying hopping parameters such that we create distinct topological regimes. One method is to assemble two different hopping probabilities $\{t_1, t_2\}$ to the lattice connections. In order to preserve the inversion symmetry of the plaquette we have to consider a larger unit cell with 6 sites (in the original lattice these will correspond to two A, B and C sites). Using OBC such that we have a system with integer number of plaquettes will result in the creation of two distinct topological regimes. In one of these, when $t_1 > t_2$, an isolated $4\times$ degenerate state appears between the two bands and the correspondent amplitude distribution mapped in the lattice shows localization at the 4 corners of the system (see Fig.3.7). The total of degenerate states gives the possibilities of changing the phase between corners, revealing all combinations of parity values in both x and y directions. This "corner state" reflects the C_4 symmetry preserved in the lattice, independently of $\{t_1, t_2\}$.

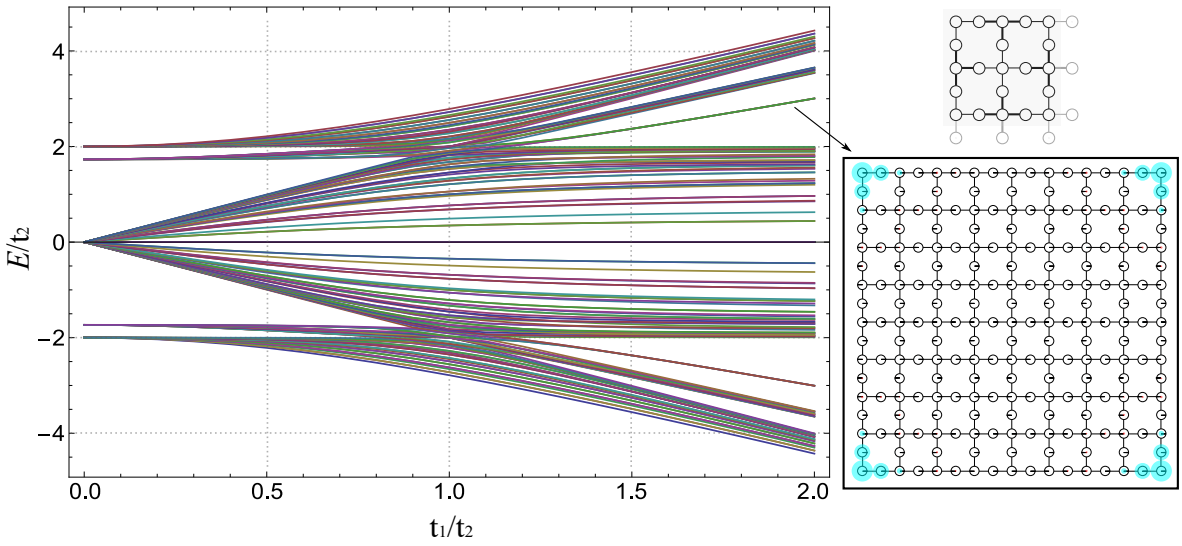

Figure 3.7: Energy spectrum as a function of the hopping parameter for the 8×8 Lieb lattice with integer number of plaquettes. The results were obtained for $t_2 = 1$. We find two isolated energy levels (with $E > 0$ and $E < 0$) crossing the bandgap when $t_1/t_2 > 1$. In the bottom-right we illustrate the correspondent eigenfunction (the size of the circles represent the amplitude of the eigenfunction in a particular site) observing a high degree of localization at the corners of the lattice. The decaying of the wavefunction into the bulk increases with t_1/t_2. In the top-right, we display the Lieb lattice with the introduction of the distinct hopping parameters t_1 (thin line) and t_2 (thick line) and we see that this modification on the Lieb model requires the unit cell to have 6 sites.

We may perform adjustments in the boundary conditions for this last system so that, in conjunction with the varying hopping parameters, we attain more states that are topologically compelling in a way that additional distinct topological regimes with isolated states emerge. For this purpose, we change our (x, y) boundary directions doing a $\pi/4$ rotation to our frame of reference. In other words, we consider the boundaries that diagonally cross the Lieb plaquettes (see red dashed lines in Fig.3.8). The resulting rotated Lieb lattice with integer number of plaquettes display two types of rotational symmetry according to the values of the hopping parameters – a 2-fold rotational symmetry whenever $t_1 \neq t_2$ and a recovering 4-fold rotational symmetry when reaching $t_1 = t_2$ – and the states will translate this change in symmetries. As an example, we examine the states of 5×5 rotated Lieb lattice by adjusting the Hamiltonian of Eq.3.2 so that we are able to reach numerical values for the amplitude distribution of the eigenfunctions mapped into the lattice. We then proceed to classify the different states in terms of the localization in real space, as the following:

- bulk states: the wavefunction is localized in the bulk of the lattice and generate bands with all possible k values which satisfy the OBC (black line in Fig.3.8);
- vertical edge states: nearly zero amplitude in the bulk and finite amplitude mostly localized in the three outer sites of the left and right vertical edges (purple line in Fig.3.8);
- horizontal edge states: nearly zero amplitude in the bulk and finite amplitude mostly localized in the three outer sites of the top and bottom horizontal edges (blue line in Fig.3.8);
- circular edge states: nearly zero amplitude in the bulk and finite amplitude mostly localized in the three outer sites of the four edges of the lattice. This particular type of state combines vertical and horizontal states with even and odd parity (yellow line in Fig.3.8);
- corner states: nearly zero amplitude in the bulk and finite amplitude mostly localized

in the three outer sites of the corners (red line in Fig.3.8).

This classification is realized in the plot of Fig.3.8 for three values of t_1/t_2. In a first approach, we can state that both corner and circular states only appear when $t_1 = t_2$. Provided that these states have 4-fold rotational symmetry, they should not be expected to appear in a regime where $t_1 \neq t_2$ since this configuration breaks C_4 class. Nevertheless, the fact that the symmetry is reduced to a C_2 for this regime allows the formation of both vertical and horizontal edge states, contrarily to the previous system in Fig.3.7. Further analysis in the following chapters will show that circular edge states are the combination of both vertical and horizontal edge states, while corner states arise from the transition between them.

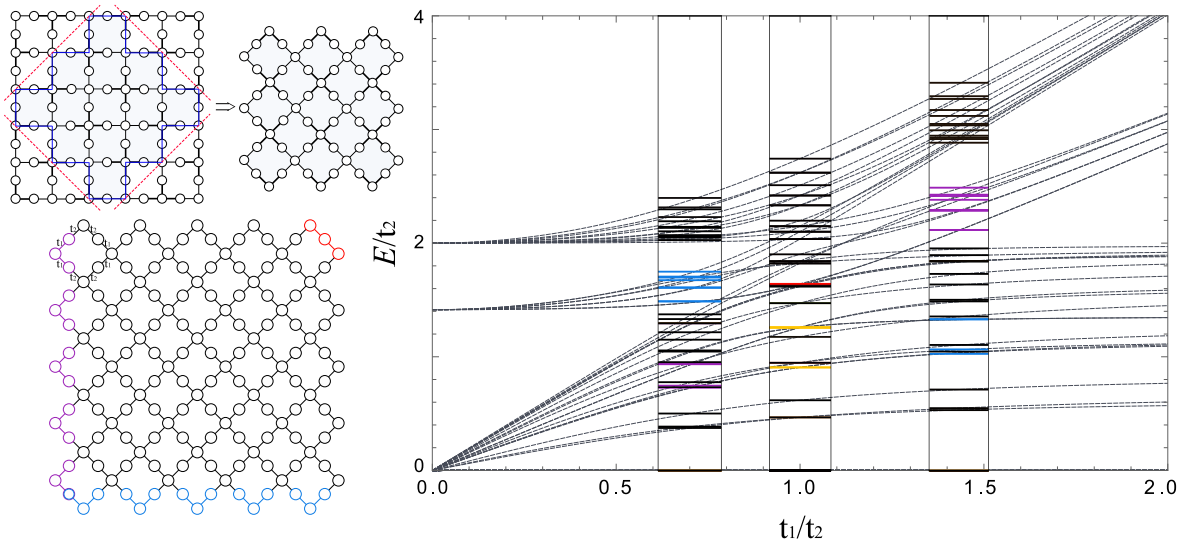

Figure 3.8: Boundary states of the Lieb rotated lattice. In the top-left, we schematize the creation of the rotated lattice from the two-dimensional Lieb model where the boundaries belong to a $\pi/4$ rotated $x - y$ reference frame. The C_4 rotation symmetry is restored when $t_1 = t_2$. The energy spectrum as a function of the hopping parameters is plotted for the 5×5 rotated Lieb lattice with integer number of plaquettes. The results were taken for $t_2 = 1$. For $t_1/t_2 = \{1/\sqrt{2}, 1, \sqrt{2}\}$, we identify the different types of states according to their localization in the lattice: bulk (black line), vertical (purple line), horizontal (blue line), corner (red line) and cirular (yellow line) states.

Chapter 4
Lieb based quasi-1D chain

In order to fully comprehend the topological transitions and emergence of edge states in the Lieb lattice we start by focusing on lower dimensional systems consisting of chains of connected plaquettes. For a Lieb ladder (consisting of a horizontal/vertical strip of square plaquettes) however, the unit cell differs from the Lieb lattice and the M_x (reflection in the x-direction) symmetry is broken. Therefore, the topological information of the lower dimensional system is not expected to be identical to the characterization of the Lieb lattice since the two models are not physically equivalent, from the symmetry point of view. On the other hand, the quasi-1D system arising from the rotated model - the Lieb rhombi chain - will still maintain both reflection symmetries and thus studying this system topology will allow us to comprehend the different types of edge states identified in Fig.3.8.

In this chapter, we analyse the Lieb rhombi chain performing a simple mapping in order to separate the overlapping of energy bands and identify the topological non-trivial transitions. The appearance of edge states is discussed with the implementation of the properties of the topological invariants introduced in Chapter 2. Specifically, we characterize the system using the definition of the chiral operator in the edge subspace introduced in Sec.2.2.2 and calculate the corrected Zak's invariant of Eq.2.23 as an identifying result of the bulk bands giving rise to the edge states in the finite chain. Finally, the relevance of the OBC is treated using the bulk-boundary correspondence approach in Sec.4.3.

We begin by examining the bulk properties of the Lieb rhombi chain composed by connected Lieb rotated plaquettes with 7 sites per unit cell (see Fig.4.1). The bulk Hamiltonian is followed by

$$H_k = \begin{bmatrix} 0 & t_1 & t_1 & e^{-ik}t_1 & e^{-ik}t_1 & 0 & 0 \\ t_1 & 0 & 0 & 0 & 0 & t_2 & 0 \\ t_1 & 0 & 0 & 0 & 0 & 0 & t_2 \\ e^{ik}t_1 & 0 & 0 & 0 & 0 & t_2 & 0 \\ e^{ik}t_1 & 0 & 0 & 0 & 0 & 0 & t_2 \\ 0 & t_2 & 0 & t_2 & 0 & 0 & 0 \\ 0 & 0 & t_2 & 0 & t_2 & 0 & 0 \end{bmatrix}. \tag{4.1}$$

The correspondent eigenvalues are written as

$$\{\epsilon_k\} = \Bigg\{0, \pm\sqrt{2}t_2, \pm\sqrt{\left(2t_1^2+t_2^2\right) - \sqrt{4t_1^2t_2^2\cos(k)+4t_1^4+t_2^4}}, \\ \pm\sqrt{\left(2t_1^2+t_2^2\right) + \sqrt{4t_1^2t_2^2\cos(k)+4t_1^4+t_2^4}}\Bigg\}. \tag{4.2}$$

Fig. 4.2a evaluates the behaviour of these bands with respect to k for fixed hopping terms $t_1 = t_2 = 1$. In this situation, we will have three flat bands with $\epsilon_k = \{0, \pm\sqrt{2}\}$ and bands touching for the specific momenta $k = \{0, \pi\}$. For the particular case of the touching point at $k = 0$, we see an independence on the values of $\{t_1, t_2\}$ and further analysis suggests that this point is robust against perturbations that preserve the inversion symmetry. The same does not manifest for $k = \pi$ since the band crossing of bands 5 (3) and 7 (1) is only seen for

the particular case of $t_1 = t_2/\sqrt{2}$, which in turn indicates we are lying in the symmetry point where a gap closes and possible edge states emerge when considering OBC.

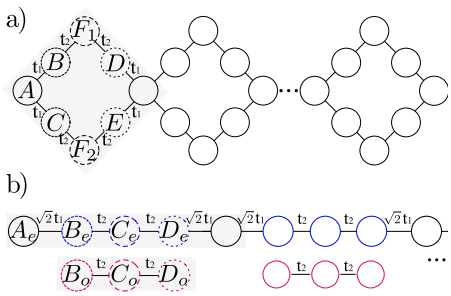

Figure 4.1: Lieb rhombi chain with 7 sites per unit cell. a) original model; b) mapped version of the vertical bonding and anti-bonding combination basis with a continuous chain in the even subspace and decoupled chains in the odd subspace.

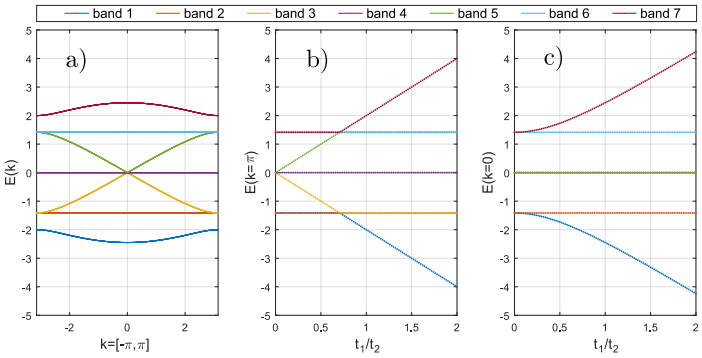

Figure 4.2: Dependence of the Lieb rhombi chain band structure with the hopping parameters. In a) we plot the band structure for $t_1 = t_2 = 1$ and in b) and c) plots we show the dependence with t_1/t_2 of the $k = \pi$ and $k = 0$ levels, respectively. The band crossing at $t_1/t_2 = 1/\sqrt{2}$ makes $k = \pi$ the state involved in the topological transition.

For the purpose of studying the edge phenomena, we perform a mapping of the system into a 1D chain (Fig.4.1b), with the application of a basis rotation. We make use of bonding and anti-bonding combinations in the finite direction with relation to the horizontal reflection axis so that the Lieb chain is mapped into a $\sqrt{2}t_1 t_2 t_2 \sqrt{2}t_1$ chain and a set of decoupled three-site clusters $t_2 t_2$. These two systems are equivalent to the Lieb chain in what concerns the band structure and each energy band can be assigned to one of the former systems such that the dispersionless bands 2,4 and 6 of $\epsilon_k = \{-\sqrt{2}t_2, 0, \sqrt{2}t_2\}$ are a result of the discontinuous cluster. Moreover, we also find an equivalence in the eigenvectors (through an inverse transform, we can reach the eigenvectors of the original system), meaning the presence of edge states ad the respective topological characterization in the mapped version can be translated into the original system. This way, for a clearer understanding, the subsequent study of the edge states will be conducted in the mapped version of Fig.4.1b.

4.1 Chiral operator in the edge subspace

Sec.2.2.2 gives the general conditions for the determination of a chiral operator that correctly describes protected edge states in a one-dimensional system. Once we successively formulated a 1D mapping of the Lieb chain with identical band structure, we may define a chiral operator that describes both the edge states of the mapped chain and, through transformation, the Lieb chain. We start by considering the continuous $\sqrt{2}t_1 t_2 t_2 \sqrt{2}t_1$ chain with 4 sites per unit cell. In analogy with the SSH model, we may search for states with a decaying behaviour in the infinite chain

$$|u_j\rangle = c^j \begin{pmatrix} \psi_{A_e} \\ \psi_{B_e} \\ \psi_{C_e} \\ \psi_{D_e} \end{pmatrix}. \tag{4.3}$$

These states, although not normalizable, will have amplitude nodes in sites corresponding to virtual sites of a open chain so that they remain eigenstates of the OBC system. From the

eigenvalue relations, we may write

$$\epsilon \begin{bmatrix} \psi_A \\ \psi_B \\ \psi_C \\ \psi_D \end{bmatrix} = \begin{bmatrix} 0 & \sqrt{2}t_1 & 0 & \sqrt{2}t_1 c^{-1} \\ \sqrt{2}t_1 & 0 & t_2 & 0 \\ 0 & t_2 & 0 & t_2 \\ \sqrt{2}t_1 c & 0 & t_2 & 0 \end{bmatrix} \begin{bmatrix} \psi_A \\ \psi_B \\ \psi_C \\ \psi_D \end{bmatrix}, \tag{4.4}$$

leading to the following set of energies (assuming the hopping parameters are real)

$$\{\epsilon_i\} = \Bigg\{ \pm \sqrt{c^2\left(2t_1^2+t_2^2\right) - \sqrt{c^3\left(2ct_1^2+t_2^2\right)\left(ct_2^2+2t_1^2\right)}}/c, \\ \pm \sqrt{c^2\left(2t_1^2+t_2^2\right) + \sqrt{c^3\left(2ct_1^2+t_2^2\right)\left(ct_2^2+2t_1^2\right)}}/c \Bigg\}. \tag{4.5}$$

The eigenvectors can be written as a function of the correspondent energy eigenvalue as

$$|u_j\rangle = K(j) \begin{bmatrix} \epsilon(\epsilon^2-2) \\ t(\epsilon^2+c-1) \\ t\epsilon(1+c) \\ t(c\epsilon^2-c+1) \end{bmatrix}, \tag{4.6}$$

with $K(j) = c^j/\epsilon(\epsilon^2-2)$ and assuming $t = \sqrt{2}t_1/t_2$ and $t_2 = 1$. Note that, for degenerate states, we may have indeterminations, so we should treat these cases using limits. Imposing OBC such that these eigenvectors are also eigenstates of the open chain implies forcing one of the amplitudes (correspondent to sublattice of the virtual site) to vanish. We reach the set of total solutions $\{c\} = \{-1, 1, -t^2, -1/t^2\}$. Not all of these solutions are relevant cases of edge states for the open chain. For instance, when $c \in \{1, -1\}$, we will get a standing wave with respective $k \in \{0, \pi\}$ (considering a unit cell with four sites). Replacing the values of c in the matrix of Eq.4.4 and finding the eigensystem of the edge-like states (for a generic unit cell j) in the open chain, one has

$$c = 1 \quad \longrightarrow \quad \begin{cases} \epsilon_1 = 0, \\ \epsilon_2 = 0, \\ \epsilon_3 = -\sqrt{2}\sqrt{t^2+1}, \\ \epsilon_4 = \sqrt{2}\sqrt{t^2+1}, \end{cases} \quad \longrightarrow \quad \begin{cases} |\epsilon_1\rangle = (0,-1,0,1)^T \\ |\epsilon_2\rangle = \left(-\frac{1}{t},0,1,0\right)^T \\ |\epsilon_3\rangle = \left(-\frac{\sqrt{2}t}{\sqrt{t^2+1}},1,-\frac{\sqrt{2}}{\sqrt{t^2+1}},1\right)^T \\ |\epsilon_4\rangle = \left(\frac{\sqrt{2}t}{\sqrt{t^2+1}},1,\frac{\sqrt{2}}{\sqrt{t^2+1}},1\right)^T \end{cases} \tag{4.7}$$

$$c = -1 \quad \longrightarrow \quad \begin{cases} \epsilon_1 = -\sqrt{2}, \\ \epsilon_2 = \sqrt{2}, \\ \epsilon_3 = -\sqrt{2t}, \\ \epsilon_4 = \sqrt{2t}, \end{cases} \quad \longrightarrow \quad \begin{cases} |\epsilon_1\rangle = \left(0,1,-\sqrt{2},1\right)^T \\ |\epsilon_2\rangle = \left(0,1,\sqrt{2},1\right)^T \\ |\epsilon_3\rangle = \left(\sqrt{2},-1,0,1\right)^T \\ |\epsilon_4\rangle = \left(-\sqrt{2},-1,0,1\right)^T \end{cases} \tag{4.8}$$

$$c = -t^2 \quad \longrightarrow \quad \begin{cases} \epsilon_1 = -\sqrt{t^2+1}, \\ \epsilon_2 = -\sqrt{t^2+1}, \\ \epsilon_3 = \sqrt{t^2+1}, \\ \epsilon_4 = \sqrt{t^2+1}, \end{cases} \quad \longrightarrow \quad \begin{cases} |\epsilon_1\rangle = \left(\frac{1}{t\sqrt{t^2+1}},0,-\frac{1}{\sqrt{t^2+1}},1\right)^T \\ |\epsilon_2\rangle = (0,0,0,0)^T \, {}^1 \\ |\epsilon_3\rangle = \left(-\frac{1}{t\sqrt{t^2+1}},0,\frac{1}{\sqrt{t^2+1}},1\right)^T \\ |\epsilon_4\rangle = (0,0,0,0)^T \, {}^1 \end{cases} \tag{4.9}$$

$$c=-1/t^2 \longrightarrow \begin{cases} \epsilon_1=-\sqrt{t^2+1}, \\ \epsilon_2=-\sqrt{t^2+1}, \\ \epsilon_3=\sqrt{t^2+1}, \\ \epsilon_4=\sqrt{t^2+1}, \end{cases} \longrightarrow \begin{cases} |\epsilon_1\rangle=\left(t,-\sqrt{t^2+1},1,0\right)^T \\ |\epsilon_2\rangle=(0,0,0,0)^T \text{ [1]} \\ |\epsilon_3\rangle=\left(t,\sqrt{t^2+1},1,0\right)^T \\ |\epsilon_4\rangle=(0,0,0,0)^T \text{ [1]}. \end{cases} \tag{4.10}$$

From these results, we may state that, in order for the edge states with $c=\{-t^2,-1/t^2\}$ to be eigenstates of the open chain, we will only arrive at edge states when the OBC are such that the virtual sites are B_e or D_e atoms. For instance, if we choose a B_e virtual site, then the edge state will have a decay of $c=-t^2$ with energy $\epsilon=\pm\sqrt{t^2+1}$ and an eigenstate obtained from substitution in Eq.4.6 as

$$|u_j,v_{B_e}\rangle=K(j)\begin{bmatrix} \pm\sqrt{t^2+1}(t^2-1) \\ 0 \\ \mp\sqrt{t^2+1}(t^2-1)t \\ t-t^5 \end{bmatrix}. \tag{4.11}$$

Once the value j of the unit cell conventionally increases from left to right then $c^j=(-t^2)^j$ will give a left (right) edge state for $\sqrt{2}t_1<t_2$ ($\sqrt{2}t_1>t_2$).

In the same manner, a D_e virtual site will have energy $\epsilon=\pm\sqrt{t^2+1}$ and decay $c=-1/t^2$ which will result in a right (left) edge state for $\sqrt{2}t_1<t_2$ ($\sqrt{2}t_1>t_2$). Accordingly, the eigenstate reads

$$|u_j,v_{D_e}\rangle=K(j)\begin{bmatrix} \pm\sqrt{t^2+1}(t^2-1) \\ (t^4-1)/t \\ \pm(t^2-1)\sqrt{t^2+1}(t^2-1)/t \\ 0 \end{bmatrix}. \tag{4.12}$$

In resemblance with the SSH model, these edge states are eigenstates of a chiral-like operator with eigenvalues $\mathbf{c}=\pm1$. To find the matrix representation of this operator in the edge state subspace, we should make use of 4 orthogonal edge states. Provided that the chiral operator should be identical for $c=-1/\bar{t}^2$ and $c=-\tilde{t}^2$, where $\tilde{t}=1/\bar{t}$, we may replace the hopping constants (we will only deal with positive values since negative values can be absorbed using a gauge transformation) in the edge eigenstates using $\bar{t}=1/\sqrt{|c|}$ and $\tilde{t}=\sqrt{|c|}$. Assuming the chiral eigenvalues of $\mathbf{c}=-1$ for $|u_j,v_D\rangle$ and $\mathbf{c}=+1$ for $|u_j,v_B\rangle$ we make use of the eigenvalue equation of the chiral operator to arrive at

$$\hat{\mathcal{C}}(c)=\begin{bmatrix} 0 & 0 & -1/\sqrt{|c|} & 0 \\ 0 & -1 & 0 & 0 \\ -\sqrt{|c|} & 0 & 0 & 0 \\ 0 & 0 & 0 & 1 \end{bmatrix}. \tag{4.13}$$

In the same way that in the SSH model the edge state remains at zero energy as long as chiral symmetry is not broken, this chiral-like operator in the edge subspace will protect the edge states, which follow the characteristic energy curve $\pm\sqrt{t^2+1}$, from mixing with bulk states. Although we looked for states with zero components in one sublattice for the purpose of finding the edge subspace, these states are still eigenstates of the infinite chain and so the chiral operator is also defined in the infinite chain. Indeed, this matrix also applies to the finite chain granted the virtual sites are both B_e or D_e atoms. Exceptionally, if we have different virtual sites in the ends of the chain, we may have a reflection of the decaying wave

[1] These states do not have physical meaning.

onto the opposite end of the chain and the chiral operator may be redefined. Nevertheless, this finite size effect can be neglected for longer chains.

As a remark, we could have also defined the chiral operator using the Bloch subspace. For this situation, we select the 4 bands that have continuity at the transition point where the edge states emerge in the open chain. Subsequently, we write the chiral operator for the infinite chain as a pairing operation between these bands as in Eq.2.48. Lastly, the chiral operator in the Wannier basis for the infinite chain is written using $\hat{\mathcal{C}} = M^{\dagger} \cdot \hat{\mathcal{C}}(k) \cdot M$ with M being the transformation matrix in the k-space basis to the Wannier basis. The result will give a chiral matrix with k-dependence and states with opposite momenta will not have identical chiral operation. This means that $\hat{\mathcal{C}}$ obtained from PBC will not be the same as $\hat{\mathcal{C}}$ for the harmonic states of the open chain. Still, the chiral operator obtained in the Bloch subspace agrees with the one determined from the edge states in the symmetry point $\sqrt{2}t_1 = t_2$ since $\hat{\mathcal{C}}(k)$ must have a continuous evolution around this point. Note that, by changing the basis we get

$$\hat{\mathcal{C}}(k) \begin{bmatrix} \psi_{A,k} \\ \psi_{B,k} \\ \psi_{C,k} \\ \psi_{D,k} \end{bmatrix} = \frac{1}{\sqrt{N}} \hat{\mathcal{C}}(k) \sum_j e^{ikj} \begin{bmatrix} \psi_{A,j} \\ \psi_{B,j} \\ \psi_{C,j} \\ \psi_{D,j} \end{bmatrix} = \frac{1}{\sqrt{N}} \sum_j e^{ikj} \hat{\mathcal{C}}(k) \begin{bmatrix} \psi_{A,j} \\ \psi_{B,j} \\ \psi_{C,j} \\ \psi_{D,j} \end{bmatrix}. \tag{4.14}$$

Thus, the generalized matrix representation will be block diagonal and each block is equal to $\hat{\mathcal{C}}(k)$ as previously stated in Eq.2.25.

In analogy with the previous case we may describe the chiral operation in the subspace of the edge states for the decoupled three site clusters $t_2 t_2$ (see Fig.4.2). These states arise from the boundary conditions applied. Indeed, when the OBC are such that a two site cluster is generated at one end of the chain, edge states appear with energy $\epsilon = \pm t_2$. Moreover, when a single site cluster is constructed, we will also have an edge state with zero energy, despite not being protected against perturbations since it overlaps with other zero flat bands present in the system. Defining the chiral operator for this cluster should be straightforward, if we think of this system as a limiting case of the previous analysis. This is, we make use of chain $t_3 t_2 t_2 t_3$ with t_3 being a hopping term which connects consecutive clusters to an additional zero amplitude site and consider the limiting case $t_3 \to 0$. Additional considerations must be taken, if we wish to use the eigenstates of Eq.4.7. Firstly, we should substitute $t = t_3/t_2 \to 0$ and recognize that ψ_{A_o} may vanish. In fact, we should drop this component in the definition of the eigenvectors in order to correctly describe the original chain. Secondly, once $t_3 \to 0$ and subsequently $t_3 < t_2$, the edge states will be localized in a single unit cell – in $j = 1$ (left) if $c = -t^2$ and in $j = N$ (right) if $c = -1/t^2$ – and the eigenvectors should be introduced in the order of the components of the non-vanishing unit cell. With the application of these conditions, we get the eigensystem

$$\begin{matrix} c = -t^2 \\ t \to 0 \end{matrix} \longrightarrow \begin{cases} \epsilon_1 = -|t_2|, \\ \epsilon_2 = -|t_2|, \\ \epsilon_3 = |t_2|, \\ \epsilon_4 = |t_2|, \end{cases} \longrightarrow |\epsilon_i\rangle = \begin{pmatrix} \psi_{B_o,j=1} \\ \psi_{C_o,j=1} \\ \psi_{D_o,j=1} \\ \psi_{A_o,j=2} \end{pmatrix} \to \begin{cases} |\epsilon_1\rangle = (0,-1,1,0)_L^T \\ |\epsilon_2\rangle = (0,0,0,0)_L^T \ {}^1 \\ |\epsilon_3\rangle = (0,1,1,0)_L^T \\ |\epsilon_4\rangle = (0,0,0,0)_L^T \ {}^1 \end{cases} \tag{4.15}$$

$$\begin{matrix} c=-1/t^2 \\ t\to 0 \end{matrix} \longrightarrow \begin{cases} \epsilon_1=-|t_2|, \\ \epsilon_2=-|t_2|, \\ \epsilon_3=|t_2|, \\ \epsilon_4=|t_2|, \end{cases} \longrightarrow |\epsilon_i\rangle = \begin{pmatrix} \psi_{A_o,j=1} \\ \psi_{B_o,j=1} \\ \psi_{C_o,j=1} \\ \psi_{D_o,j=1} \end{pmatrix} \to \begin{cases} |\epsilon_1\rangle = (0,-1,1,0)^T_R \\ |\epsilon_2\rangle = (0,0,0,0)^T_R{}^1 \\ |\epsilon_3\rangle = (0,1,1,0)^T_R \\ |\epsilon_4\rangle = (0,0,0,0)^T_R{}^1. \end{cases} \tag{4.16}$$

Indeed, $\psi_{A_o} \to 0$ when considering the limit $t \to 0$ and we may eliminate this component from the eigenvectors so that the respective edge eigensystem for the three site cluster reads

$$c\to 0^- \longrightarrow |\epsilon_i\rangle = \begin{pmatrix} \psi_{B_o} \\ \psi_{C_o} \\ \psi_{D_o} \end{pmatrix}_{j=1} \to \begin{cases} |\epsilon_1\rangle = (0,-1,1)^T_R \\ |\epsilon_2\rangle = (0,0,0)^T_R{}^1 \\ |\epsilon_3\rangle = (0,1,1)^T_R \\ |\epsilon_4\rangle = (0,0,0)^T_R{}^1 \end{cases} \tag{4.17}$$

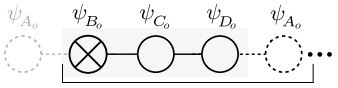

$$c\to -\infty \longrightarrow |\epsilon_i\rangle = \begin{pmatrix} \psi_{B_o} \\ \psi_{C_o} \\ \psi_{D_o} \end{pmatrix}_{j=N} \to \begin{cases} |\epsilon_1\rangle = (-1,1,0)^T_R \\ |\epsilon_2\rangle = (0,0,0)^T_R{}^1 \\ |\epsilon_3\rangle = (1,1,0)^T_R \\ |\epsilon_4\rangle = (0,0,0)^T_R{}^1 \end{cases} \tag{4.18}$$

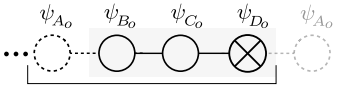

In a first analysis, we see that replacing the obtained c values in the matrix of Eq.4.13 generate infinite terms. Thus, the chiral operator cannot be directly obtained by the c substitution. Still, by inspection, the matrix representation of the chiral operator in the subspace of the above edge states, dropping the added extra A_o sites, can be written for components B_o and D_o, with the condition that $|\psi_{C_o}| = \max(\psi_{B_o}, \psi_{D_o})$, as

$$\hat{\mathcal{C}}(c) = \begin{bmatrix} -1 & 0 \\ 0 & 1 \end{bmatrix}. \tag{4.19}$$

where the edge states are eigenstates of $\hat{\mathcal{C}}(c)$ with eigenvalues $\mathbf{c} = 1$ for the right edge and $\mathbf{c} = -1$ for the left edge. This chiral operator will protect the edge states with $\epsilon = \pm t_2$ arising from the open boundary conditions that select left B_o or right D_o virtual sites.

The original Lieb chain is a superposition of behaviours of the previous chains. In the continuous chain, both the value of t and the boundary conditions determine the appearance of edge states. For the decoupled cluster, the topological transition occurs for $t_2 = t_3 = 0$ and edge states will only be dependent on the choice of virtual sites, provided that the hopping terms are positive. Moreover, fixing a C-virtual site will generate a zero energy state which falls into the respective flat band.

4.2 Determination of the Zak's phase

Commonly, robust topological boundary states often appear in a gap that lies above bands adding up to a quantized topological index [45]. According to Section 2.1.2, some 1D systems do not possess a well quantized topological invariant and, in the case of the Zak's phase, this is due to the fact that the inversion symmetry does not lie in the middle of any choice of unit cell. As seen in Fig.4.3, the Lieb system is a good candidate for the application of the corrected Zak's phase expressed in Eq.2.23 with additional considerations as we are dealing

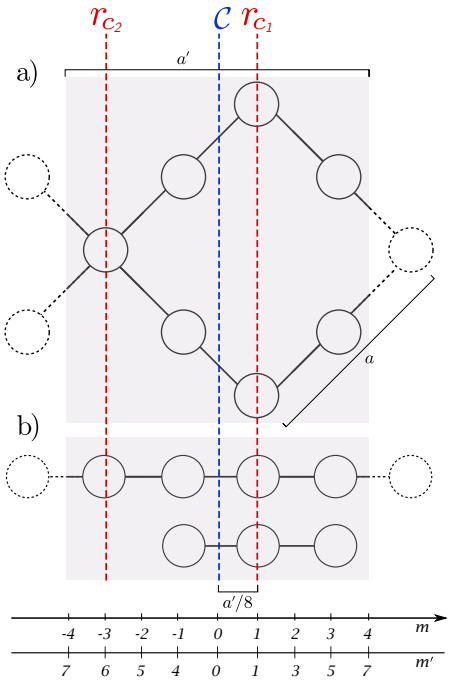

Figure 4.3: Determination of index m' for the calculation of the Zak's phase. We specify the unit cell centre (blue line) as well as the two possible inversion centre axis (red line) for both the original a) and mapped b) rhombi chain.

		r_{c_1}			r_{c_2}		
	band	$\tilde{\mathcal{Z}}_j$	p_0	p_π	$\tilde{\mathcal{Z}}_j$	p_0	p_π
$t_1 < t_2/\sqrt{2}$	1	0	1	1	π	1	-1
	2	0	1	1	π	1	-1
	3	π	1	-1	0	1	1
	4	0	-1	-1	π	-1	1
	5	0	-1	-1	π	-1	1
	6	0	1	1	π	1	-1
	7	0	1	1	π	1	-1
$t_1 > t_2/\sqrt{2}$	1	π	1	-1	0	1	1
	2	0	1	1	π	1	-1
	3	0	1	1	π	1	-1
	4	0	-1	-1	π	-1	1
	5	π	-1	1	0	-1	-1
	6	0	1	1	π	1	-1
	7	π	1	-1	0	1	1

Table 4.1: Calculation of the Zak's phase ($\mathcal{Z}_j$) and parity values p_0 and p_π for each band j numbered in Fig.4.2 considering the identified topological regimes and the two possible inversion centres r_{c1} and r_{c2}.

with a quasi-1D system. We may choose the inversion centre $r_c = a(1/2 + m/2N_x)$ with $N_x = 4$ being the number of sites encountered in the x-direction of the $\sqrt{2}t_1t_2t_2\sqrt{2}t_1$ mapped chain and m the displacement of the inversion axis with respect to the centre of the unit cell. We may choose one of the two axis r_{c1} or r_{c2} with respective $m = 1$ and $m = -3$. The limits of the sum in the expression of the corrected Zak's phase should also be modified. Due to the fact that, in certain situations, the inversion axis contain more than one site, the displacement parameter m no longer reflects the number of k-dependent terms in the inversion operator or equivalently, the number of sites moving to a different unit cell when performing an inversion operation. Therefore, the Zak's phase for the Lieb chain may be expressed in terms of the sign of m as

$$\mathcal{Z}_j = \begin{cases} \arg\left(p_0 p_\pi^\dagger\right) + \sum_{N-m'+1}^{N} \int_0^\pi dk |u_j(k, |m'|)|^2, & m < 0, \\ \arg\left(p_0 p_\pi^\dagger\right) - \sum_{1}^{m'} \int_0^\pi dk |u_j(k, |m'|)|^2, & m > 0, \end{cases} \tag{4.20}$$

where m' is the evaluated number of k-dependent terms for each displacement m and $N = 7$ the number of sites in the unit cell of the Lieb chain.

We gather the results for the Zak's phase of each band in Table 4.1 taking into account the two topological regimes previously mentioned. From one regime to the other we see a π shift on the Zak's phase in the non flat bands which correspond to the continuous chain in the 1D mapping and is consistent with the results achieved for a $t_1t_1t_2t_2$ chain in [28]. This phase shift is due to the opening of the gap in Fig.4.2b. We see that bands 1(5) and 3(7)

are degenerate at $k = \pi$ in the regime $t_1 < t_2/\sqrt{2}$ and split when $t_1 = t_2/\sqrt{2}$. In this case, a perturbation to the unit cell is generated when we move away from the topological transition, reducing the symmetry of the system and thus introducing a gap in these folded bands. On the other hand, since there is no gap opening or closing for the other high symmetry point $k = 0$, the parity values p_0 for each band remain constant for the two dimerization regimes. For the flat bands which arise from the three dangling sites, the two different regimes will not introduce a π-shift because the choice of unit cell will preserve this discontinuous chain. This reflects the fact that the topological transition for this chain of clusters occurs when $t_3 = 0$. If, for instance, we choose a different unit cell which does not contain three connected dangling sites, a topological transition will appear and the Zak's phase is shifted by π.

Considering the same regime, the Zak's phases for the two inversion axis suffer a π shift:

$$\tilde{\mathcal{Z}}_{j,r_{c2}} - \tilde{\mathcal{Z}}_{j,r_{c1}} = arg(p_0 p_\pi) + \sum_{m=2}^{7} \int_0^\pi dk |u_j(k,m)|^2 - arg(p_0 p_\pi) + \sum_{m=1} \int_0^\pi dk |u_j(k,m)|^2 = \\ = \int_0^\pi dk \sum_{m=1}^{7} |u_j(k,m)|^2 = \pi. \quad (4.21)$$

Let us look at the consequences from changing the dimerization and, at the same time, changing the inversion axis. We see that only the flat bands have a π shift. These flat bands are originated from the three dangling sites in the effective 1D mapping of the Lieb chain. If, for instance we replace $\sqrt{2}t_1 \leftrightarrow t_2$ and change the inversion axis $r_{c1} \leftrightarrow r_{c2}$, the $\sqrt{2}t_1 t_2 t_2 \sqrt{2}t_1$ chain will remain the same. However, for the three site chain, since there is only one hopping parameter in these dangling sites, the hopping transformation will not change the Zak's phase since there is no topological transition between dimerization regimes. The π phase is only introduced when we change the inversion axis. For these dangling sites, the inversion operator due to r_{c1} remains k-independent and for r_{c2} all the terms in the matrix become k-dependent. So the difference between the two Zak phases gives π in the particular case of the flat bands.

4.3 Bulk-boundary correspondence

In this section, we make a connection between the topological properties emerged from the chiral symmetry and inversion symmetry and the appearance of edge states in the respective open system, maintaining the study of the Lieb chain mapped into the two 1D chains. We start by addressing the possible OBC which, in the $\sqrt{2}t_1 t_2 t_2 \sqrt{2}t_1$ chain gather 10 different boundaries (granted that the left and right directions for the endings are physically indistinguishable). We present 8 of these cases in Table 4.2 since the other cases are equivalent in a $t_1 \leftrightarrow t_2$ transformation (although not all cases have remain invariant under this transformation when the three site cluster is considered, but the results can still be extrapolated). These 8 cases are divided into two left ends – $\sqrt{2}t_1 t_2$ and $\sqrt{2}t_1 \sqrt{2}t_1$ – spanning through the 4 different right endings for each. For each open $\sqrt{2}t_1 t_2 t_2 \sqrt{2}t_1$ chain, we give the correspondent endings for the 3-site cluster and evaluate the conditions for the presence of both edge states and $k = \{0, \pi\}$ states. Note that, in the finite case, we will not be able to construct harmonic states with $k = \{0, \pi\}$ ($c = \{1, -1\}$) since they are invariant under inversion operation. Nevertheless, these k states will appear if the virtual sites are positioned in the same sublattice as the zero amplitude nodes.

In the last column of Table 4.2, we investigate if the effect of a $\sqrt{2}t_1 \leftrightarrow t_2$ (and $t_3 \leftrightarrow t_2$ in the cluster) transformation leaves invariant the respective open chain, that is, if the edge states and direction of localization will prevail when inverting the hopping amplitudes. Note that, in this operation the dimerization regimes will also invert.

Left end	Right end	Energy plot over t	Coments	$\leftrightarrow$
t_1t_2 virtual D_e	t_1t_1 virtual C_e	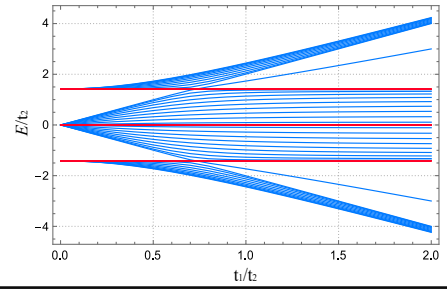	Left edge state for $t_1 > t_2$ evolving from $k = \pi$ state with $\epsilon = \pm\sqrt{2}t$	Yes
t_3t_2 virtual A_o	t_3t_3 virtual A_o		No edge states since $\psi_{A_o} = 0$ is imposed	No
t_1t_2 virtual D_e	t_1t_2 virtual D_e	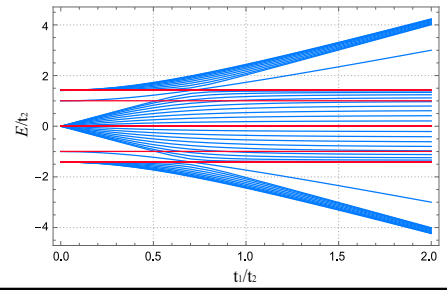	Left edge state for $t_1 > t_2$ and right edge state for $t_1 < t_2$. No $k = \{0, \pi\}$ states	Yes
t_3t_2 virtual A_o	t_3t_2 virtual D_o		Right edge state for $t_2 > 0$ with $\epsilon = \pm\lvert t_2\rvert = 1$	Yes
t_1t_2 virtual D_e	t_2t_2 virtual A_e	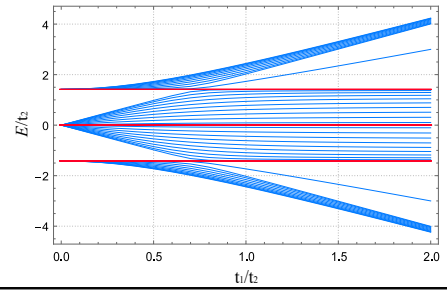	Left edge state for $t_1 > t_2$ evolving from $k = \pi$ state with $\epsilon = \pm\sqrt{2}$	Yes
t_3t_2 virtual A_o	t_2t_2 virtual A_o		No edge states since $\psi_{A_o} = 0$ is imposed	No
t_1t_2 virtual D_e	t_2t_1 virtual B_e	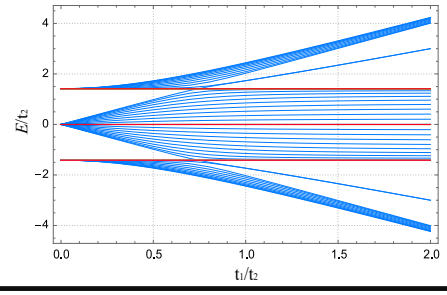	Both left and right edge states emerge when $t_1 > t_2$. No $k = \pi$ state	Yes
t_3t_2 virtual A_o	t_2t_3 virtual A_o		No edge states since $\psi_{A_o} = 0$ is imposed	No
t_1t_1 virtual C_e	t_1t_1 virtual C_e	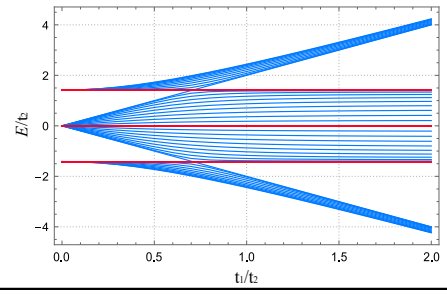	No edge states. $k = \pi$ state with $\epsilon = \pm\sqrt{2}t$ and $k = 0$ state with $\epsilon = 0$	Yes
t_3t_3 virtual A_o	t_3t_3 virtual A_o		No edge states since $\psi_{A_o} = 0$ is imposed	Yes
t_1t_1 virtual C_e	t_1t_2 virtual D_e	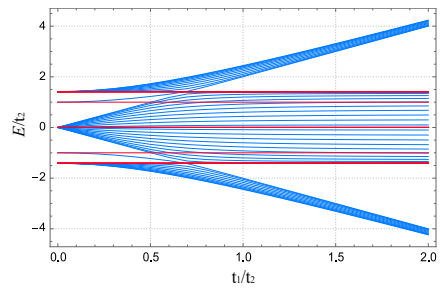	Right edge state for $t_1 < t_2$ evolving to $k = \pi$ state of $\epsilon = \pm\sqrt{2}t$	Yes
t_3t_3 virtual A_o	t_3t_2 virtual D_o		Right edge state for $t_2 > 0$ with $\epsilon = \pm\lvert t_2\rvert = 1$	No

Left end	Right end	Energy plot over t	Coments	$\leftrightarrow$
t_1t_1 virtual C_e	t_2t_2 virtual A_e	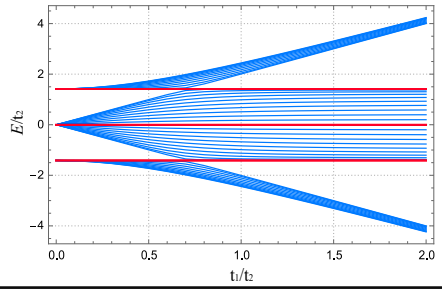	No edge states. $k = \pi$ state with $\epsilon = \pm\sqrt{2}$ ($\epsilon = \pm\sqrt{2}t$) for $t_1 < t_2$ ($t_1 > t_2$)	Yes
t_3t_3 virtual A_o	t_2t_2 virtual A_o		No edge states since $\psi_{A_o} = 0$ is imposed	Yes
t_1t_1 virtual C_e	t_2t_1 virtual B_e	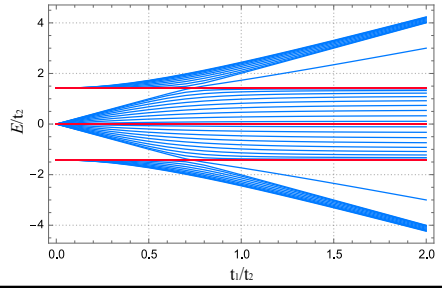	Right edge state for $t_1 > t_2$ evolving from $k = \pi$ with $\epsilon = \pm\sqrt{2}$	Yes
t_3t_3 virtual A_o	t_2t_3 virtual A_o		No edge states since $\psi_{A_o} = 0$ is imposed	No

Table 4.2: Bulk boundary correspondence for each termination of the mapped Lieb rhombi chain. The energy spectrum is separated by colours representing the continuous chain (blue) and the disconnected clusters (red). The last collumn evaluates whether the open system is invariant under $\sqrt{2}t_1 \leftrightarrow t_2$ transformation. We have replaced $\sqrt{2}t_1 \to t_1$.

In the open $\sqrt{2}t_1t_2t_2\sqrt{2}t_1$ chain, both the emergence and localization of edge states will depend on the value of t and type of OBC provided – a virtual site D_e in the right (left) end and $\sqrt{2}t_1 < t_2$ ($\sqrt{2}t_1 > t_2$) leads to a right (left) edge state with $c = -1/t^2$ and a virtual site B_e in the right (left) end and $\sqrt{2}t_1 > t_2$ ($\sqrt{2}t_1 < t_2$) leads to a right (left) edge state with $c = -t^2$. Otherwise, instead of the appearance of edge states, we will have $k = \pi$ state with energy $\epsilon = \pm\sqrt{2}$ for a A_e virtual site and $\epsilon = \pm\sqrt{2}t$ for a C_e virtual site. In situations where mixed endings are revealed, such as chain $\sqrt{2}t_1\sqrt{2}t_1 \cdots t_2\sqrt{2}t_1$, a k state may appear in one of the two regimes of t evolving from/to an edge state.

Earlier, we used the $\sqrt{2}t_3t_2t_2\sqrt{2}t_3$ chain to discover the form of edge states in the discontinuous three-site cluster, using the limit $t_3 \to 0$. As previously stated, we verify that the presence of these edge states is only dependent on the choice of virtual site. In addition, since the transition point is at $t_2 = 0$ and our analysis is taken for positive values of the hopping terms, a single right D_o or left B_o virtual site is the only condition necessary for the appearance of edge states of $\epsilon = \pm|t_2|$. Recall that a left D_o or a right B_o are not possible virtual sites as they are "connected" to the chain by a vanishing hopping term t_3.

From the $\sqrt{2}t_1 \leftrightarrow t_2$ transformation we see that, while in the $\sqrt{2}t_1t_2t_2\sqrt{2}t_1$ chain the system remains equivalent with respect to the edge states appearance and localization, the same is not valid for the 3-site cluster. The reason is that, whenever the first (last) hopping terms in the $\sqrt{2}t_1t_2t_2\sqrt{2}t_1$ chain are $t_2\sqrt{2}t_1$ ($\sqrt{2}t_1t_2$) we will have an edge state in the 3-site cluster. So, upon transformation, we will witness the appearance/disappearance of the $\epsilon = \pm|t_2|$ edge states. The transformation will only leave the system invariant when: 1) changing the hopping terms is equivalent to switching directions; 2) both original and transformed chains have inversion symmetry. These two properties can be seen in chains $\sqrt{2}t_1t_2 \cdots \sqrt{2}t_1t_2$, $\sqrt{2}t_1\sqrt{2}t_1 \cdots t_2t_2$ and $\sqrt{2}t_1\sqrt{2}t_1 \cdots \sqrt{2}t_1\sqrt{2}t_1$.

Chapter 5
Lieb-type systems: from the ribbon to the square lattice

With the purpose of understanding how the findings of the Lieb rhombi chain translate into the Lieb lattice, we consider an enlarged system consisting of vertically connected Lieb rhombi chains and examine its topological transitions and the form of the edge states in finite conditions. Subsequently, a comparison between the ribbon with PBC in one direction and the square lattice is conducted applying PBC. With this, we aim to explain the different types of boundary states in the Lieb rotated lattice and their topological behaviour.

5.1 Lieb rhombi ribbon

The simplest Lieb rhombi ribbon consists of two rhombi chains connected in a F-site. The Hamiltonian for this system can be determined using Eq.4.1 and adjusting for the ribbon with 15 sites per unit cell. This will result in diagonally replicating the matrix of Eq.4.1 with the addition of hopping terms to connect the two plaquettes. Next, we introduce two possible mappings aiming for the simplification of the model.

5.1.1 Symmetry based mapping

Looking at the $2\times$ rotated Lieb chain of Fig.5.1, we recognize the existence of a reflection symmetry with respect to the horizontal axis placed in the middle of the two plaquettes. A possible mapping for this model can be done using a basis of states with even and odd parity values with respect to this symmetry axis. This basis of bonding and anti-bonding states reads

$$|\psi_{Ie/o}\rangle = \begin{cases} \frac{1}{\sqrt{2}}(|\psi_I\rangle \pm \hat{R}\,|\psi_I\rangle), & |\psi_I\rangle \neq \hat{R}\,|\psi_I\rangle\,, \\ |\psi_I\rangle\,, & |\psi_I\rangle = \hat{R}\,|\psi_I\rangle\,. \end{cases} \tag{5.1}$$

where $\hat{R}$ is the reflection operation. We rewrite the Hamiltonian of the $2\times$ rotated Lieb chain in this basis and get two decoupled smaller chains. In the odd subspace, a $t_1t_2t_2t_1$ chain is generated with two additional sites connected to A-sites which can be again combined into a bonding and anti-bonding state (see Fig.5.1). Consequently, the anti-bonding state will be disconnected from the chain and generate a flat band of zero energy and the bonding state still connected to the chain generates an effective momentum dependent local potential at site A. In the even subspace, we get a chain similar to the Lieb rotated chain with the exception that the hopping terms connected to sites intersecting the reflection axis in the original system suffer a re-normalization.

For both systems, a zero energy flat band specific to the usual compact localized state of the Lieb lattice (see Sec.3.2.1) is present. This $4\times$ degenerate eigenstate occupies sites BC_e, CB_e, DE_e and ED_e with alternating parity values in x and y direction and zero amplitude in sites A_e, F_e and $F2_e$ responsible for the connection between plaquettes. A possible approach to simplify the even subspace Hamiltonian is to consider a new ring basis comprised of the 4 degenerate compact localized eigenstates at sites BC_e, CB_e, DE_e and ED_e. The introduction

of this basis rotation in the Hamiltonian generates the system illustrated in Fig.5.1. In the vertical direction, the current model resembles an AB_2 chain – a quasi-1D lattice composed of an array of quantum rings with 4 sites [46, 47] – where each plaquette holds modified hopping terms. The negative hopping term in both rings generates a Peierls phase factor of $e^{i\pi}$ so that the total magnetic flux across the plaquette is $\Phi = \pi$. The band structure for this system is not fully described by flat bands due to the different hopping terms in the chain and the zero energy state has an extended localized eigenfunction exhibiting finite amplitudes at sites connecting the plaquettes in the x-direction. Nonetheless, for each subset of two plaquettes in the y-direction, we notice the existence of a compact localized state manifesting the Aharonov-Bohm caging effect where a loaded particle remains confined due to destructive interference [7, 45].

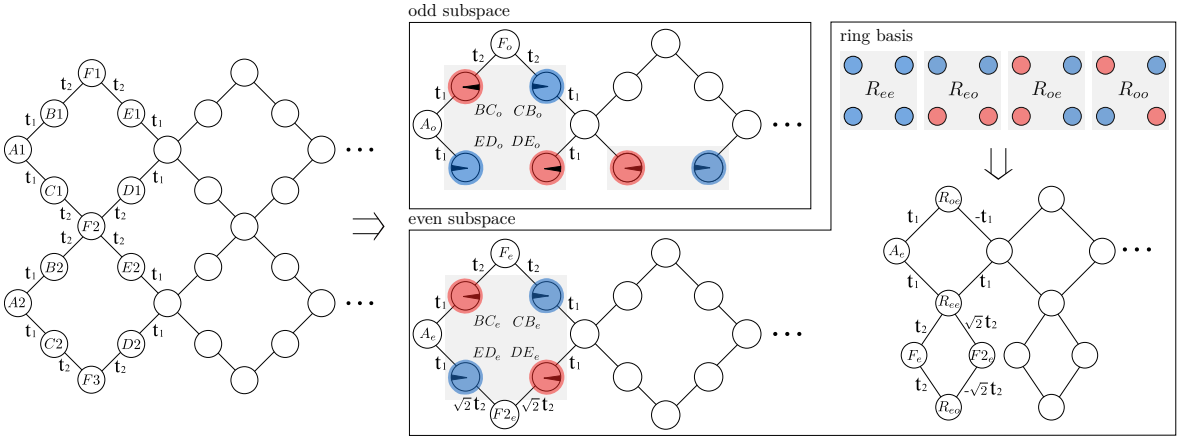

Figure 5.1: Symmetry based mapping in the Lieb rhombi ribbon. From the bonding and anti-bonding combination of Eq.5.1, we separate the two mappings into odd and even subspaces, where the latter can be further simplified considering a ring basis of 4 sites. The resulting system resembles the AB_2 chain and may display localized states emerging from the Aharonov-Bohm caging effect. Red and blue circles represent the eigenfunction site amplitudes having 0 and π phases, respectively.

5.1.2 Vertical combination mapping

In similarity with the Lieb chain we may perform a basis rotation of the $2\times$ rotated Lieb chain evenly combining the sites that intersect the same vertical axis and satisfying the orthogonality rule. The new basis for each vertical combination will have dimension equal to the number of sites in that vertical axis. The basis space for each vertical axis α $B_{I\alpha} = \{|\psi_{I1}\rangle, \ldots, |\psi_{IN}\rangle\}$ is found using the conditions:

$$\begin{cases} |\psi_{Ii}\rangle = \dfrac{1}{\sqrt{\beta}} \displaystyle\sum_{m=1}^{\beta} a_m \, |\psi_{Im}\rangle \,, \\ a_m^* a_m = 1, \forall m = 1, \ldots, \dim \mathcal{S}_\alpha, \quad \text{if } \dim \mathcal{S}_\alpha \text{ is even}, \\ \langle \psi_{Ii} \,|\, \psi_{Ij} \rangle = 0, \quad i \neq j, \\ N = \dim \mathcal{S}_\alpha, \\ \beta = \dim \mathcal{S}_\alpha, \quad \text{if } \dim \mathcal{S}_\alpha \text{ is even}, \end{cases} \tag{5.2}$$

where $\mathcal{S}_\alpha$ is the group of all I_m sites in the vertical axis α. For example, a vertical axis with 4 sites will have a basis space with dimension $N = 4$ vectors, each with equal unitary amplitude components $a_m = \pm 1$ such that all 4 vectors of the basis for that axis α are orthogonal. For an odd number of vertical sites in the basis, the components were chosen to

be the smallest integer amplitudes possible, respecting the vertical reflection symmetry. Using the adjusted Hamiltonian of Eq.4.1 we get the mapped system, in 5.2, of two chains with a sequence of hopping constants of $\sqrt{2}t_1\sqrt{3/2}t_2\sqrt{3/2}t_2\sqrt{2}t_1$ and $\sqrt{2}t_1\sqrt{1/2}t_2\sqrt{1/2}t_2\sqrt{2}t_1$. The inversion centre sites of each individual chain carries additional connected sites that generate effective energy dependent onsite potentials. These two mapped systems will display their own characteristic energy bands and possible crossing among levels of different chains, when the hopping terms are changed, are irrelevant for the topological characterization since the systems are physically independent. Likewise, and in resemblance with the former rotated Lieb system, each chain will hold a topological regime where edge states emerge.

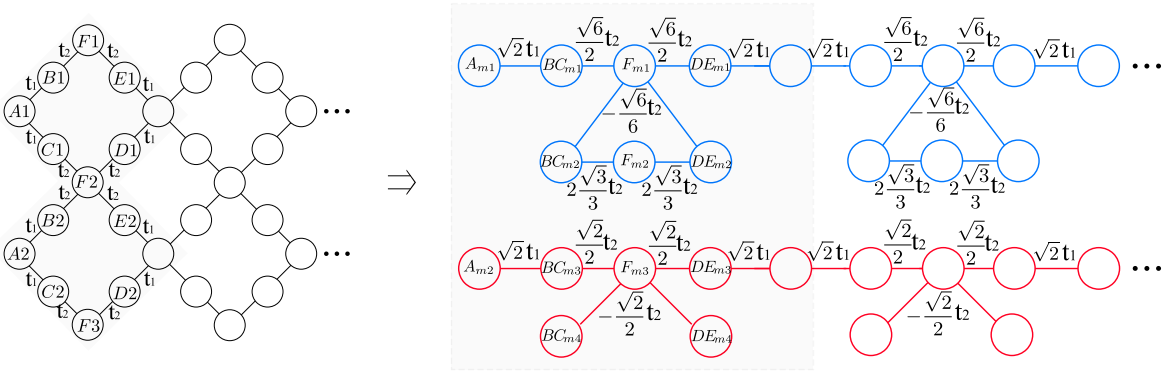

Figure 5.2: Vertical combination mapping in the Lieb rhombi ribbon. We achieve two continuous chains, $\sqrt{2}t_1\sqrt{3/2}t_2\sqrt{3/2}t_2\sqrt{2}t_1$ and $\sqrt{2}t_1\sqrt{1/2}t_2\sqrt{1/2}t_2\sqrt{2}t_1$, with additional t_2-dependent clusters connected to the "middle" site of the unit cell.

In Fig.5.3, we plot the energy levels as a function of the original hopping terms $\{t_1, t_2\}$ for a 2× Lieb ribbon with integer number of plaquettes (virtual sites left-DE and right-BC) and where the levels corresponding to each chain are separated by colours. From this choice of OBC, two isolated levels (with symmetric energies) appear between bands in the regime $t_1 \gg t_2$ and both appear at the level crossing of the two top/bottom bands for the blue levels and of the two middle bands for the red levels. Further analysis of the eigenfunctions for this system indicate that these states have finite amplitudes in the two boundaries of the open system in the left of Fig.5.2 and are approximately 2x-degenerated with parity switch in the x-direction. Additionally, the higher energy blue edge state has even parity while the lower red edge state has odd parity in the y-direction. Since they are distinguishable by colour in the energy spectrum, these states are localized in the boundaries of each of the 1D open chains and the topological transition is given by the ratio between the hopping amplitudes for the given chain, as in the previous section. In this case however, to calculate the point of transition we need to take into account the effect of the sites connected to the middle point of the unit cell and rewrite an effective linear chain with corrected hopping amplitudes, as illustrated in Fig.5.3.

We start by writing the tight-binding equations for the amplitudes of relevant sites in systems *i1)* and *ii)*

$$i1)\begin{cases} \epsilon\psi_a = \widetilde{t_2}(\psi_L + \psi_R) - \widetilde{t_3}(\psi_b + \psi_d), \\ \epsilon\psi_{b,d} = -\widetilde{t_3}\psi_a + \widetilde{t_4}\psi_c, \\ \epsilon\psi_c = -\widetilde{t_4}(\psi_b + \psi_d), \\ \epsilon\psi_L = -\widetilde{t_1}\psi_{L-1} + \widetilde{t_2}\psi_a, \\ \epsilon\psi_R = -\widetilde{t_1}\psi_{R+1} + \widetilde{t_2}\psi_a, \end{cases} \qquad ii)\begin{cases} \epsilon\psi_{\tilde{a}} = \widetilde{t_2}^{eff}(\psi_L + \psi_R), \\ \epsilon\psi_L = -\widetilde{t_1}\psi_{L-1} + \widetilde{t_2}^{eff}\psi_{\tilde{a}}, \\ \epsilon\psi_R = -\widetilde{t_1}\psi_{R+1} + \widetilde{t_2}^{eff}\psi_{\tilde{a}}, \end{cases} \tag{5.3}$$

where ψ_α is the wavefunction amplitude on site α and ϵ is the state energy. From the second and third equations of system *i1)* we write $\psi_b + \psi_d = -2\widetilde{t_3}\psi_a/(\epsilon - 2\widetilde{t_4}^2/\epsilon)$ which allows to express the amplitude equation for site a as

$$\left(\epsilon - \frac{2\widetilde{t_3}^2}{\epsilon - 2\widetilde{t_4}^2/\epsilon}\right)\psi_a = \widetilde{t_2}(\psi_L + \psi_R). \tag{5.4}$$

Using the last two equations of both systems, we get the relation between the amplitudes at both sites a and $\tilde{a}$ as $\epsilon\psi_{\tilde{a}} = \widetilde{t_2}\psi_a/\widetilde{t_2}^{eff}$. Finally, dividing the first equation from system *ii)* by Eq.5.4, we get the expression for the effective hopping amplitude of the transformed chain as a function of the energy as

$$\widetilde{t_2}^{eff} = \widetilde{t_2}\sqrt{\frac{\epsilon^2 - 2\widetilde{t_4}^2}{\epsilon^2 - 2\widetilde{t_4}^2 - 2\widetilde{t_3}^2}}. \tag{5.5}$$

Substituting the hopping parameters, $\widetilde{t_1} = \sqrt{2}t_1$, $\widetilde{t_2} = \sqrt{6}t_2/2$, $\widetilde{t_3} = \sqrt{6}t_2/6$, $\widetilde{t_4} = 2\sqrt{3}t_2/3$ and since the energy where the levels cross is close to $\epsilon \simeq \pm 2.16$, we obtain $\widetilde{t_2}^{eff} \simeq 1.3417t_2$. The point of transition of the edge state in the blue line of Fig.5.3 is given by the ratio

$$\frac{t_1}{t_2} = \frac{\widetilde{t_1}/\sqrt{2}}{\widetilde{t_2}^{eff}/1.3417} \simeq 1 \tag{5.6}$$

where we have established that, for the transformed chain, the well known topological transition takes place at $\widetilde{t_1} = \widetilde{t_2}^{eff} = 1$.

The same transformation can be done for chain *i2)* and we get the following expression for the effective hopping parameter

$$\widetilde{t_2}^{eff} = \widetilde{t_2}\sqrt{\frac{\epsilon^2}{\epsilon^2 - 2\widetilde{t_2}^2}}. \tag{5.7}$$

Using $\widetilde{t_1} = \sqrt{2}t_1$, $\widetilde{t_2} = \sqrt{2}t_2/2$ and the crossing energy close to $\epsilon \simeq \pm 1.52$, we obtain the topological transition point at

$$\frac{t_1}{t_2} \simeq \frac{1}{\sqrt{2}}. \tag{5.8}$$

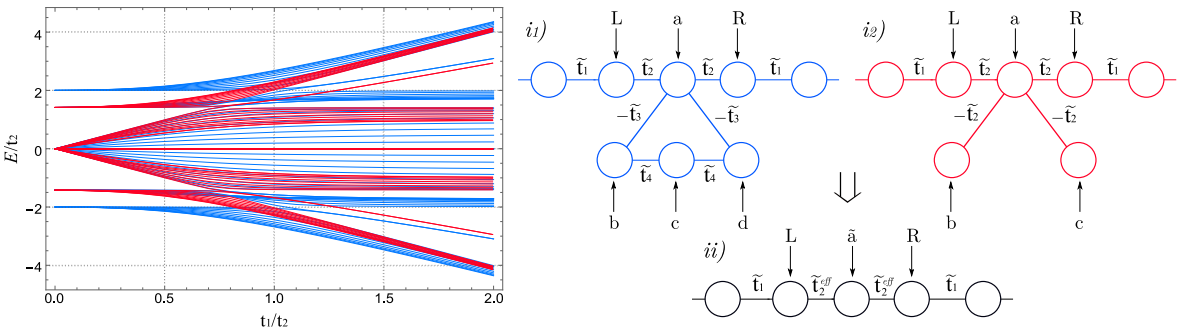

Figure 5.3: Identification of the transition points of the Lieb rhombi ribbon. Left: Energy spectrum of the Lieb rhombi ribbon separated by colours the levels corresponding to the top (blue) and bottom (red) chains of the vertical combination mapping of Fig.5.2. Right: Simplification process of the mapped chains into a $\widetilde{t_1}\widetilde{t_2}^{eff}\widetilde{t_2}^{eff}\widetilde{t_1}$ chain where the topological transition is well known and given by the ratio between the hopping parameters.

These two results in Eqs.5.6 and 5.8 are not in total agreement with the crossing points of the plot in Fig.5.3 for the emergence of isolated levels corresponding to edge states. This is due to the finite size effect which creates overlaps between wavefunctions not expected in infinite systems. Nevertheless, considering periodic boundary conditions, the transition points agree with the previous results, as seen in Fig.5.4 for $k = \pi$.

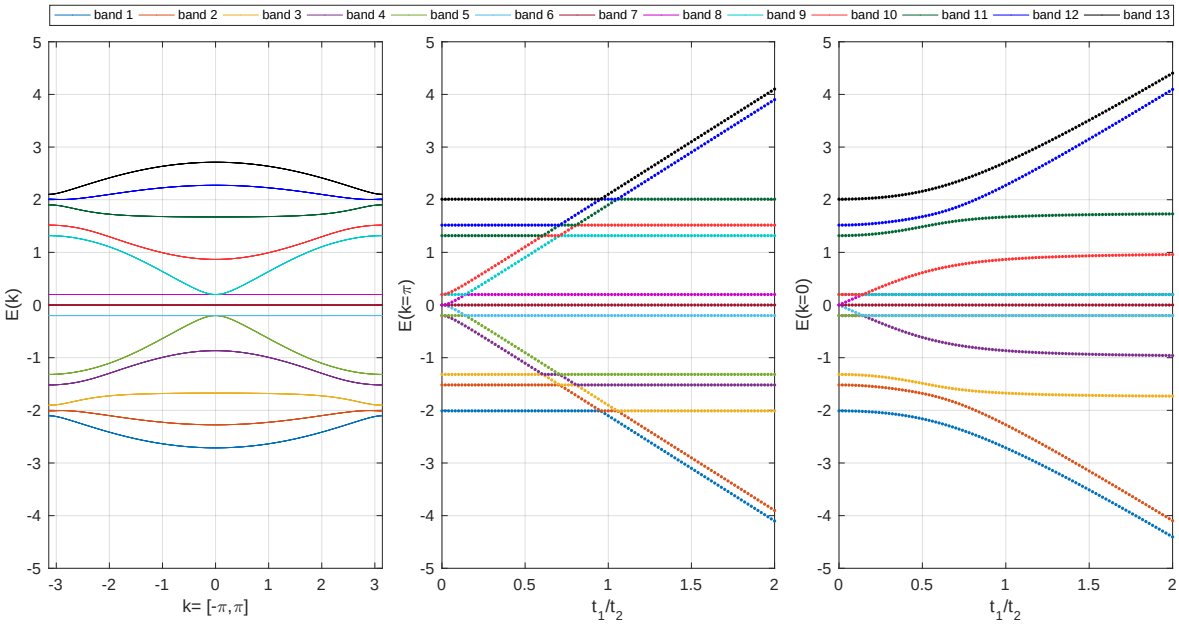

Figure 5.4: Dependence of the Lieb rhombi ribbon band structure with the hopping parameters. In the left, we plot the band structure for $t_1 = t_2 = 1$ and in the middle and right plots we see the dependence with t_1/t_2 of the $k = \pi$ and $k = 0$ levels, respectively. We identify a gap closing for $k = \pi$ at the topological transition points $t_1/t_2 = \{1, 1/\sqrt{2}\}$. Once more, $k = 0$ will not have gap closing and, for this reason, is not a k-state involved in the topological transition. The degeneracy was lifted adding two onsite potentials of $e_1 = 0.2$ in sites $\{B_1, C_1, D_1, E_1\}$ and $e_2 = -0.2$ in sites $\{B_2, C_2, D_2, E_2\}$. For the unperturbed, system the unfolded transition points overlap.

		r_{c_1}					r_{c_1}					r_{c_1}		
	band	$\tilde{\mathcal{Z}}_j$	p_0	p_π		**band**	$\tilde{\mathcal{Z}}_j$	p_0	p_π		**band**	$\tilde{\mathcal{Z}}_j$	p_0	p_π
$t_1 < t_2/\sqrt{2}$	1	0	1	1	$t_2/\sqrt{2} < t_1 < t_2$	1	0	1	1	$t_1 > t_2$	1	π	1	-1
	2	0	1	1		2	π	1	-1		2	π	1	-1
	3	0	1	1		3	π	1	-1		3	0	1	1
	4	π	1	-1		4	0	1	1		4	0	1	1
	5	0	-1	-1		5	π	-1	1		5	π	-1	1
	9	0	-1	-1		9	π	-1	1		9	π	-1	1
	10	π	1	-1		10	0	1	1		10	0	1	1
	11	0	1	1		11	π	1	-1		11	0	1	1
	12	0	1	1		12	π	1	-1		12	π	1	-1
	13	0	1	1		13	0	1	1		13	π	1	-1

Table 5.1: Calculation of the Zak's phase ($\mathcal{Z}_j$) and parity values p_0 and p_π for each band j numbered in Fig.5.4 considering the identified topological regimes and the inversion centre r_{c1}.

Having identified the regimes where a topological transition takes place, we can now calculate the corrected Zak's phase (using the method of the previous chapter) of each band in k-space (see Table 5.1), considering the preceding inversion centre r_{c1} (the other inversion

centre will simply give a π-shift in all values of the Zak's phase). The results show a phase shift in bands 2, 3, 4 and 5 (respectively 9, 10, 11 and 12 for negative energies) for the first transition and a phase shift in bands 1 and 3 (or 11 and 13 for negative energies) for the second transition. As we can see in the parity values of these bands, the modifications at the topological transitions take place for the eigenfunctions of $k = \pi$, while p_0 remains constant. This can be verified in Fig.5.4. For the evolution of t_1/t_2 the bands previously mentioned are responsible for a gap opening/closing only at the symmetry point $k = \pi$ and at the transition points $t_1/t_2 = \{1, 1/\sqrt{2}\}$.

5.2 Three plaquette Lieb rhombi ribbon

In this section, we address the Lieb rhombi ribbon with 3 plaquettes per unit cell and perform the vertical combination mapping for this chain with the purpose of finding a generalized mapping for the application on the Lieb rotated lattice.

From the outcome of Fig.5.5, we may state that: 1) an increasing number of plaquettes per unit cell will, in principle, generate additional effective chains dependent on both hopping terms that can be treated in resemblance with the previous lower dimensional cases; 2) in analogy with the Lieb rhombi chain, the existence of connected clusters depending solely on t_2 generates edge states with energies approximately independent from t_1 if the chosen OBC breaks the cluster structure in, at least, one of the terminations of the ribbon; 3) the loops created by the connected clusters can be correlated with the ring structures found in the symmetry mapping of the Lieb rhombi ribbon in the sense that certain states may display the Aharonov-Bohm caging effect if flux is introduced; 4) even though we get an extra effective chain, the computation of the band structure of the unperturbed system as a function of the hopping terms will display the identical number of band crossings in the same t_1/t_2 points as the unperturbed Lieb rhombi ribbon (see Fig.5.4). This may be due to the fact that two effective chains are connected through a loop cluster and therefore, the eigenfunctions for each chain will be dependent as long as $t_2 \neq 0$. In fact, this dependence suggests the possibility of a further mapping which gather these two continuous chain into a single one and, naturally, we obtain only two effective chains each with a topological transition point. Still, if we perform a perturbation to the system such that the degeneracy of the bands is removed whilst preserving the symmetries, we find a "cascade" of topological transitions lying in the surroundings of the prior calculated transition points. Moreover, the positions of these unfolded transition points can be manipulated modifying the value of the onsite potentials considered in the perturbation.

From the comparison of the mapping results for both the two and three plaquette rhombi ribbons, we understand that a generalized mapping for a n-number of plaquettes per unit cell may not be straightforward. Indeed, both the number of effective chains and the form of the clusters can not be inferred solely based on these two examples. Moreover, the increased complexity of the mapped three plaquette rhombi ribbon is a discouraging fact for the application to the mapping approach for the Lieb lattice.

5.3 Lieb rhombi ribbon with single-direction PBC

In the view of understanding the types of boundary states in the Lieb rotated lattice, we first introduce the periodic boundary conditions in one direction, with the intention of reducing the amount of variables that have to be resolved when considering the higher dimension model. Notably, the resultant solutions should, in principle, be qualitatively similar

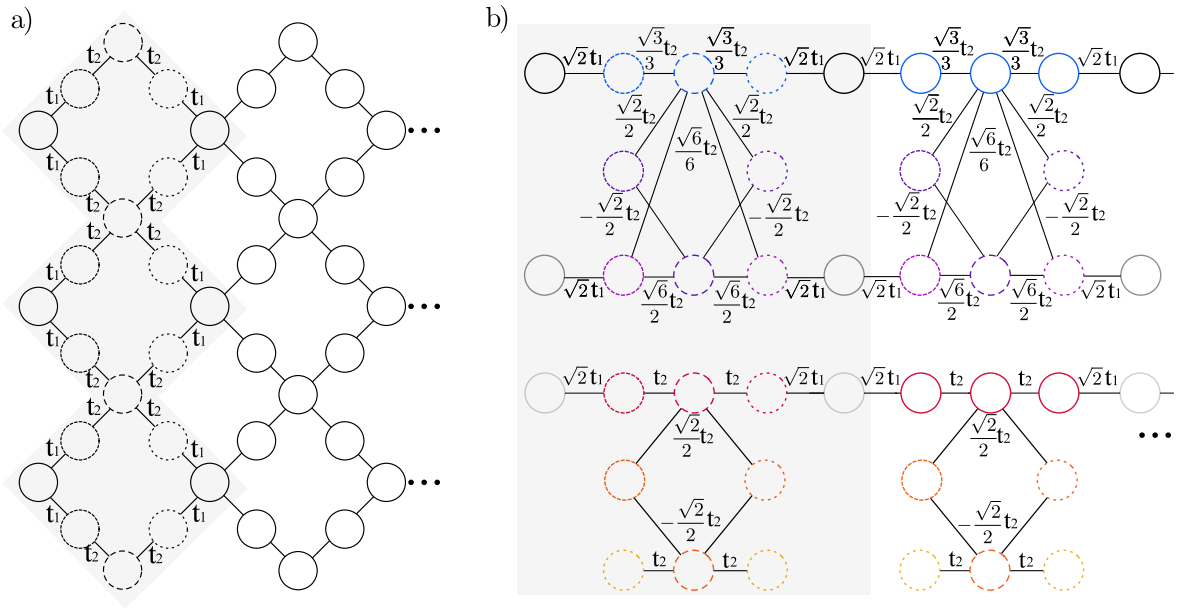

Figure 5.5: Vertical combination mapping for the Lieb rhombi ribbon with 3 plaquettes per unit cell. The increasing number of plaquettes suggest additional effective chains in the mapped model.

---

to those of the 2D lattice, at least in a sufficiently large finite system, where the effect of the boundaries can be neglected.

In this section, PBC will be applied to one of the two (x or y) directions, maintaining the other direction open. This will result in a closed rhombi ribbon cylinder and the edge states are found in the circumference of both circled bases. We first consider a horizontal cylinder where PBC are applied in the y-direction and OBC in the perpendicular direction preserving an integer number of plaquettes. In other words, and using the site notation of Fig.5.6a), this means we are choosing the virtual sites for the left and right ends to be $\{E, F\}$ and $\{B, C\}$, respectively. Recall, for the Lieb rhombi chain, that these boundaries matched the mapped $t_1 t_2 \cdots t_2 t_1$ termination, which carried both left and right edge states when $t_1 > t_2$. So, we also expect edge states to appear in this case for such topological regime. Fig.5.6 plots the energy spectrum for the ribbon considering PBC and a unit cell with 5 plaquettes in the y-direction. Indeed, the appearance of energy levels in the middle of the bandgap is only seen for the case where t_1 outgrows t_2. These gapless states are confined to the open vertical boundaries of the ribbon and, in principle, will be responsible for the vertical edge states in the square lattice. Furthermore, each energy level will correspond to an eigenstate of well-defined k-value in the y-direction, where the PBC are applied.

Giving use to these considerations, we attempt to find the analytical form of the edge-like states. Since we are dealing with a two-dimensional system, we may define two independent decaying behaviours $\{c_x, c_y\}$ such that

$$|u_{l,j}\rangle = c_x^l c_y^j \begin{pmatrix} \psi_A \\ \psi_B \\ \psi_C \\ \psi_D \\ \psi_E \\ \psi_F \end{pmatrix} \tag{5.9}$$

with indices (l, j) denoting the unit cell of 6 sites per unit cell in two-dimensional case. The Hamiltonian for the system in the edge subspace may be written using the decaying behaviour

as

$$H_c = \begin{bmatrix} 0 & t_1 & t_1 & 0 & t_1/c_x & t_1/c_x \\ t_1 & 0 & 0 & t_2 & 0 & 0 \\ t_1 & 0 & 0 & t_2 c_y & 0 & 0 \\ 0 & t_2 & t_2/c_y & 0 & t_2 & t_2/c_y \\ t_1 c_x & 0 & 0 & t_2 & 0 & 0 \\ t_1 c_x & 0 & 0 & t_2 c_y & 0 & 0 \end{bmatrix}. \tag{5.10}$$

Note that, if both c_x and c_y are $\{k_x, k_y\}$ dependent complex exponentials, then this matrix becomes the Hermitian H_k. Requesting PBC for the y-direction implies that the form of c_y must be k-dependent and we assume $c_y = e^{ik_y}$. The number of gapless energy levels will then be dependent on the supported k_y values. Moreover, $k = \{0, \pi\}$ will define the top and bottom levels of the edge states band (see Fig.5.6).

We may resolve the eigenvalue relations (equivalent to Eq.4.4) so that the form of the eigenvectors as a function of both decaying values and energy eigenvalues for a particular unit cell (l, j) is

$$|u_{l,j}\rangle = K(l,j) \begin{bmatrix} \epsilon\left(\epsilon^2 - 4\right) c_y \\ t\left(c_y\epsilon^2 + c_x + c_x c_y - 3c_y + 1\right) \\ t c_y\left(\epsilon^2 + c_x + c_x c_y + c_y - 3\right) \\ (c_x + 1)\epsilon t(c_y + 1) \\ t\left(c_x c_y \epsilon^2 + c_x - 3c_x c_y + c_y + 1\right) \\ t c_y\left(c_x\epsilon^2 - 3c_x + c_x c_y + c_y + 1\right) \end{bmatrix}. \tag{5.11}$$

For simplification purposes we set above $t_2 = 1$ and $t = t_1/t_2 = t_1$. In the particular case of $\{B, C\}$ and $\{E, F\}$ virtual sites, the solutions for the decaying behviours are accomplished by setting the amplitudes in these sublattices to zero. For $c_x \neq 0$ the results follow

$$\begin{matrix} c_y = 1 \\ c_x = -t^2 \end{matrix} \longrightarrow \begin{cases} \epsilon_1 = 0, \\ \epsilon_2 = 0, \\ \epsilon_3 = -\sqrt{2}\sqrt{t^2+1}, \\ \epsilon_4 = -\sqrt{2}\sqrt{t^2+1}, \\ \epsilon_5 = \sqrt{2}\sqrt{t^2+1}, \\ \epsilon_6 = \sqrt{2}\sqrt{t^2+1}, \end{cases} \longrightarrow \begin{cases} |\epsilon_1\rangle = (0,0,0,0,-1,1)^T \\ |\epsilon_2\rangle = (0,-1,1,0,0,0)^T \\ |\epsilon_3\rangle = \left(\frac{\sqrt{2}}{t\sqrt{1+t^2}}, 0, 0, -\frac{\sqrt{2}}{t\sqrt{1+t^2}}, 1, 1\right)^T \\ |\epsilon_4\rangle = (0,0,0,0,0,0)^T \\ |\epsilon_5\rangle = \left(-\frac{\sqrt{2}}{t\sqrt{1+t^2}}, 0, 0, \frac{\sqrt{2}}{t\sqrt{1+t^2}}, 1, 1\right)^T \\ |\epsilon_6\rangle = (0,0,0,0,0,0)^T \end{cases} \tag{5.12}$$

$$\begin{matrix} c_y = 1 \\ c_x = -1/t^2 \end{matrix} \longrightarrow \begin{cases} \epsilon_1 = 0, \\ \epsilon_2 = 0, \\ \epsilon_3 = -\sqrt{2}\sqrt{t^2+1}, \\ \epsilon_4 = -\sqrt{2}\sqrt{t^2+1}, \\ \epsilon_5 = \sqrt{2}\sqrt{t^2+1}, \\ \epsilon_6 = \sqrt{2}\sqrt{t^2+1}, \end{cases} \longrightarrow \begin{cases} |\epsilon_1\rangle = (0,0,0,0,-1,1)^T \\ |\epsilon_2\rangle = (0,-1,1,0,0,0)^T \\ |\epsilon_3\rangle = \left(t, -\frac{\sqrt{t^2+1}}{\sqrt{2}}, -\frac{\sqrt{t^2+1}}{\sqrt{2}}, 1, 0, 0\right)^T \\ |\epsilon_4\rangle = (0,0,0,0,0,0)^T \\ |\epsilon_5\rangle = \left(t, \frac{\sqrt{t^2+1}}{\sqrt{2}}, \frac{\sqrt{t^2+1}}{\sqrt{2}}, 1, 0, 0\right)^T \\ |\epsilon_6\rangle = (0,0,0,0,0,0)^T. \end{cases} \tag{5.13}$$

A $k_y = 0$ ($c_y = 1$) state will have two possible decaying behaviours in the x-direction $c_x = \{-t^2, -1/t^2\}$ depending on the hopping constants. Since we intend to study the $t > 1$ regime, then a $c_x^l = (-t^2)^l$ ($c_x^l = (-1/t^2)^l$) decaying will give a right (left) edge state in which the degree of localization will increase with t ($1/t$). In this boundary, we have established the

amplitudes of sublattices B and C (E and F) to vanish which leads to the eigenstates $|\epsilon_3\rangle$ and $|\epsilon_5\rangle$ with finite energies $\epsilon_{3,5} = \mp\sqrt{2}\sqrt{t^2+1}$.

For a non-zero c_x, the eigenfunctions will always have dependence on t_2 and hence a topological transition at a given point $t = t_1/t_2 =$ constant. The same will not be seen for $k_y = \pi$ ($c_y = -1$) where the only possible edge-like states have $c_x = 0$, which implies that the state is completely localized in a single unit cell. This result is supported by the numerical calculations of the eigenfunctions. In this situation, the states are those of a quasi-1D chain with PBC, once there are no contributions of sites from the bulk unit cells ($l, j \neq \{0, N\}$). Looking at the form of the eigenvectors for this case, given by

$$\begin{matrix} c_y = -1 \\ c_x = 0 \end{matrix} \longrightarrow \begin{cases} \epsilon_1 = -2, \\ \epsilon_2 = 2, \\ \epsilon_3 = 0, \\ \epsilon_4 = 0, \\ \epsilon_5 = -\sqrt{2}t, \\ \epsilon_6 = \sqrt{2}t, \end{cases} \longrightarrow \begin{cases} |\epsilon_1\rangle = (0,-1,1,2,-1,1)^T \\ |\epsilon_2\rangle = (0,-1,1,-2,-1,1)^T \\ |\epsilon_3\rangle = \left(0,\frac{1}{2},-\frac{1}{2},0,0,1\right)^T \\ |\epsilon_4\rangle = \left(0,-\frac{1}{2},\frac{1}{2},0,1,0\right)^T \\ |\epsilon_5\rangle = \left(-\sqrt{2},1,1,0,0,0\right)^T \\ |\epsilon_6\rangle = \left(\sqrt{2},1,1,0,0,0\right)^T, \end{cases} \tag{5.14}$$

we notice, for the particular case of $\epsilon_{5,6} = \mp\sqrt{2}t$, that the amplitude is confined to the outer sites $\{A, B, C\}$ for the left boundary (or $\{A, E, F\}$ if we change the indexation so that the unit cell is respective to the right boundary) and is zero otherwise. The fact that $\psi_D = 0$ and these sites are the nearest neighbours of the finite amplitude sites connected only by t_2 terms, the boundary becomes decoupled from the lattice and the effect of t_2 is non-existent. For this reason, we may state that the topological transition for this k_y-state occurs at $t = 0$.

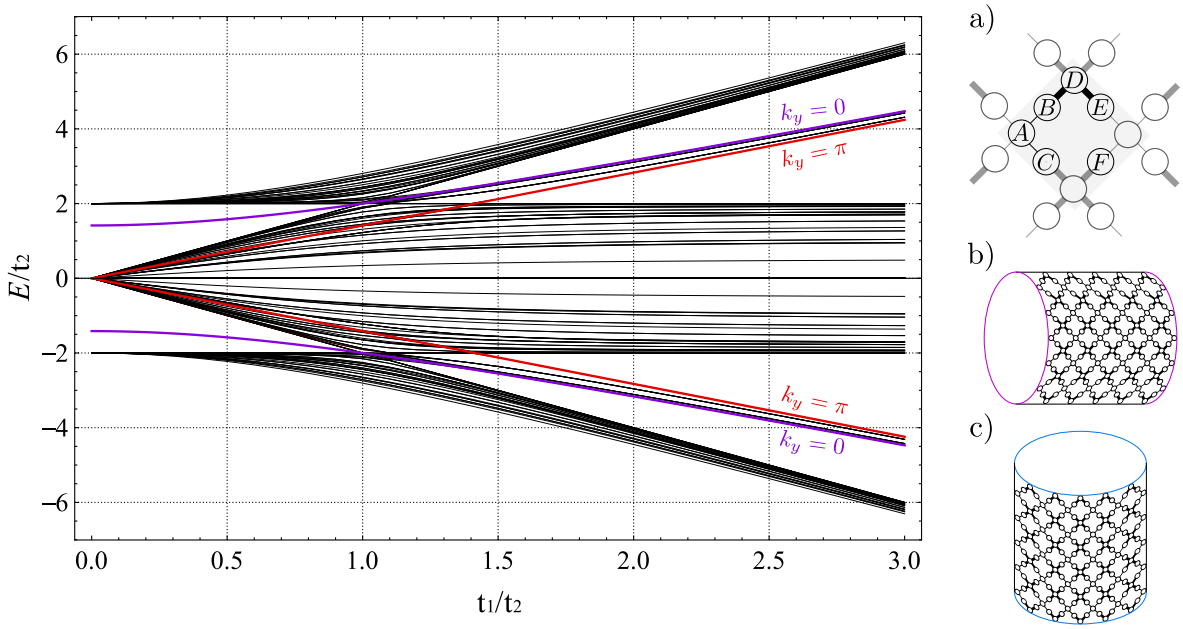

Figure 5.6: Calculation of $\{k_y\} = \{0, \pi\}$ edge states for the Lieb rhombi ribbon with PBC in the y-direction and unit cell illustrated in a) with t_1 (thin line) and t_2 (thick line) hopping terms. b) and c) schematically illustrate the PBC in the y and x direction, respectively (the colours in the boundaries of the cylinders represent the type of edge states of Fig.3.8 supported for each system). We plot the dependence of the energy spectrum with the hopping parameters for system b) and overlap the analytical form of the edge states for $k_y = 0$ (purple) and $k_y = \pi$ (blue). Due to the chosen terminations for the numerical evaluation, we will not see the $k_y = 0$ edge state in regime $t_1 < t_2$.

All these conclusions are intuitively found in the plot of Fig.5.6, where we have overlapped the eigenvalue solutions for $k_y = \{0, \pi\}$ edge states onto the numerical calculations of the Lieb rhombi ribbon with 5×5 plaquettes and PBC in the y-direction. We may state that the analytical calculation successfully describe these particular edge states. For $k_y = \pi$ we will not see a level crossing representing the topological transition, as we predicted that this will occur for $t_1 = 0$. In opposition, $k_y = 0$ energy curve (purple line) encounters a band crossing at $t_1/t_2 = 1$. For increasing values of t, this will be the point where both left and right vertical edge states will appear in the numerical results.

This procedure can be duplicated for the system of Fig.5.6c), where the PBC are applied in the x-direction. Indeed, since the horizontal open boundaries in this case end with t_2 hoppings, both the top and bottom edge states appear when $t_1 < t_2$. Thus, the analytical results can be inferred by simply take the transformation $t_1 \leftrightarrow t_2$ reaching, for $k_x \in \{0, \pi\}$ the decaying values in the y-direction of $c_y \in \{(-t^2, -1/t^2), 0\}$.

5.4 Rotated Lieb square lattice

So far, we have studied the rotated Lieb square lattice with the application of PBC to one of the boundaries of the system. With this, we have assumed a plane wave behaviour in the closed direction which allowed us to find the edge-like states in the open direction. Since the square lattice has terminations ruled by t_1 hoppings in the y-direction and t_2 hoppings in the x-direction, by studying each boundary isolated, we are also predicting the behaviour of the square lattice for both $t_1 < t_2$ and $t_1 > t_2$ regimes.

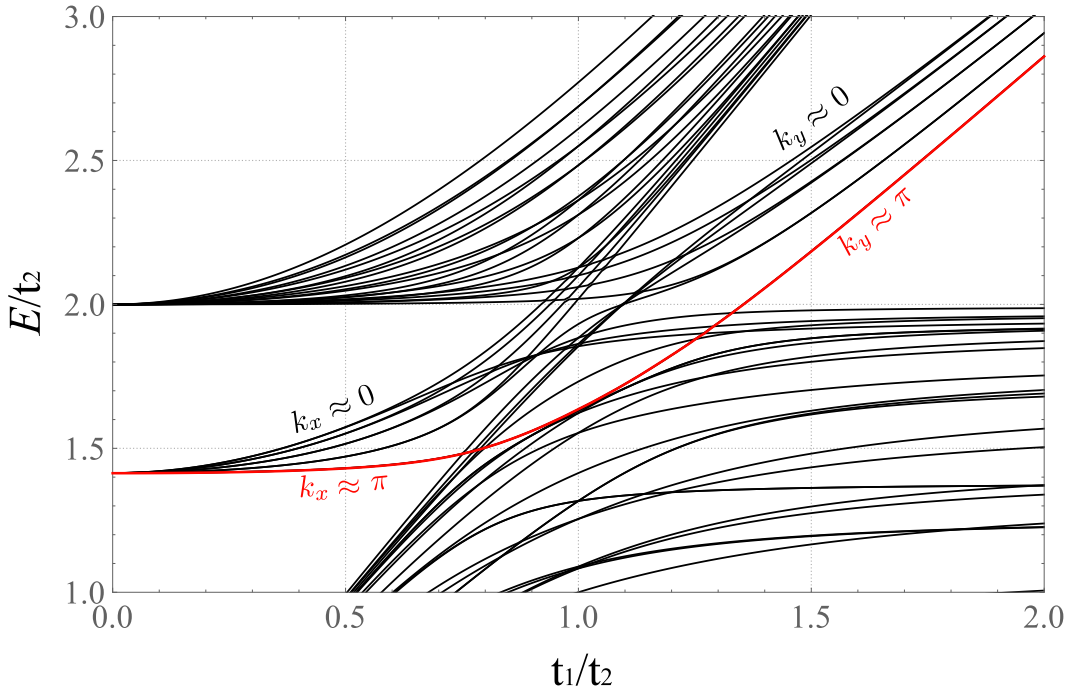

Figure 5.7: Numerical calculations of the energy spectrum for the rotated Lieb square lattice and dependence on the hopping parameters. The highlighted curve belongs to the $k_x \approx \pi$ for $t_1 < t_2$ and $k_y \approx \pi$ for $t_1 > t_2$. Corner localized modes appear for $t_1 = t_2$ in this curve.

From the numerical results of Fig.5.7, we may state that the top and bottom levels crossing the bandgap are $k_{x,y} \approx \{0, \pi\}$ states that have similar behaviour as those calculated for the PBC systems. When $t_1 > t_2$ ($t_1 < t_2$), they are localized in the vertical (horizontal)

boundaries in the x (y) direction. In the specific case of $k \approx 0$, when $t_1 > t_2$ these vertical boundary modes have a bulk oriented decay of $c_x = -t^2$ for a right localized state and $c_x = -1/t^2$ for a left localized state. In the same way, for $t_1 < t_2$, we will encounter horizontal edge states with decay $c_y = -t^2$ ($c_y = -1/t^2$) for a top (bottom) localization. We ought to focus on the highlighted edge state of Fig.5.7. This particular state drifts away from the remaining levels lying in the bandgap and touching at the topological transition point $t_1 = t_2$. From the previous results, we identify this state to be $k_{x,y} \approx \pi$ with decaying behaviour $c = 0$ for both topological regimes, meaning it is entirely localized in a single boundary (or unit cell if PBC are considered in the perpendicular direction of maximum localization). For the limiting cases $t_1 \gg t_2$ and $t_1 \ll t_2$ the energy eigenvalues found using periodic conditions $\epsilon_a = \pm\sqrt{2}t_1$ and $\epsilon_b = \pm\sqrt{2}t_2$ are good approximations for this boundary mode in the square lattice. Nevertheless, around point $t_1 = t_2$ the energy curve will, in principle, be ruled by a function $f(\epsilon_a, \epsilon_b)$. At this point, corner states are generated due to the increase in symmetry (the square lattice holds a 4-fold rotational symmetry when both hoppings are equal). Our findings allow us to conclude that this corner state is conceived from the evolution of maximum localized horizontal to vertical edge states of $k \approx \pi$ which do not fall into a topological transition point.

Chapter 6
Conclusion

In this dissertation, we studied boundary modes in Lieb-type systems (chains, ribbons and square clusters), in an effort to develop a rigorous topological description. In a first analysis, we reveal the important role played by the symmetries in the existence and protection of these boundary states. In fact, considerable differences were shown between boundaries imposed parallel to the sides of the Lieb square plaquettes and diagonally across these plaquettes. The latter case broadcast additional types of boundary states categorized by their localization in the lattice. More importantly, we have linked the topological transition point with the creation of a higher symmetry class C_{4v} where corner states emerge between topological phases ruled by C_{2v} class. Remarkably, these corner states can be experimentally realized simply by constructing a Lieb rotated square lattice with integer number of plaquettes and equal hopping parameter connecting all sites, in contradiction with the Lieb lattice with parallel boundaries, where two hopping terms have to be present.

In the pursuit of interpreting the boundary modes of the Lieb rotated lattice, we have considered two dimensional systems with PBC in the vertical and horizontal boundaries and studied the distinct topological regimes in which edge states are formed. Our results show that the combination of the edge description for the application of PBC in the x-direction for $t_1 > t_2$ and in the y-direction for $t_1 < t_2$ describes, in a good approximation, the boundary modes of the Lieb rotated square lattice for these regimes. The conducted topological characterization of the various Lieb-type systems led to the identification of two main classes of states where boundary modes arise: i) those who suffer a topological phase transition in a well defined crossing point having a clear distinction between non-trivial and trivial phases; ii) states which do not participate in the level crossing at the topological transition point and are continuously in the topological non-trivial phase due to the fact that one of the hopping terms has no effect on the state. Notably in this case, one obtains partially decoupled clusters dependent on a single hopping parameter. The latter edge state behaviour lies behind the appearance of the corner state in the Lieb rotated square lattice and is created by the transition of maximally localized horizontal to vertical edge modes.

A further prominent outcome worth mentioning is the "cascade" of topological transitions seen for increasing number of plaquettes in the unit cells of the rhombi ribbon model, when symmetry preserving onsite potentials are implemented to lift the band degeneracy. This "cascade" is equally observed in the Lieb square lattice for the topological transition point at $k \neq \pi$ and the number of these transition points increase with the lattice size. Future work should be conducted on the effects on other systems of employing these onsite potentials.

Finally, with the intention of giving support to our topological characterization, we have introduced the generalized versions of the chiral operator and the Zak's phase calculations found in the literature, and successfully applied to our systems that are comparably more complex than the usual one dimensional SSH model.

As further future work, we propose the creation of a groundwork supporting the findings of the present thesis, with the investigation of further systems that show the topological features strongly dependent on the symmetry variations of the lattice. A polarization characterization of the corner state relying on the quadrupole moment [25] may as well possess interesting quantized results. In such case, a generalization of the symmetry operations must be realized, in order to effectively describe two dimensional systems with non-centred point operations.

Bibliography

[1] Zengji Yue, Xiaolin Wang, and Min Gu. Topological insulator materials for advanced optoelectronic devices. 2018.

[2] Ching-Kai Chiu, Jeffrey C. Y. Teo, Andreas P. Schnyder, and Shinsei Ryu. Classification of topological quantum matter with symmetries. *Rev. Mod. Phys.*, 88:035005, 2016.

[3] Shun-Qing Shen, Wen-Yu Shan, and Hai-Zhou Lu. Topological insulator and the dirac equation. *Spin*, 01(01):33–44, 2011.

[4] M. Z. Hasan and C. L. Kane. *Colloquium* : Topological insulators. *Rev. Mod. Phys.*, 82:3045–3067, 2010.

[5] Xiao-Liang Qi and Shou-Cheng Zhang. Topological insulators and superconductors. *Rev. Mod. Phys.*, 83:1057–1110, 2011.

[6] Michel Fruchart and David Carpentier. An introduction to topological insulators. *Comptes Rendus Physique*, 14:779 – 815, 2013.

[7] Zhongbo Yan and Shaolong Wan. Topological phases, topological flat bands, and topological excitations in a one-dimensional dimerized lattice with spin-orbit coupling. *EPL (Europhysics Letters)*, 107(4):47007, 2014.

[8] W. P. Su, J. R. Schrieffer, and A. J. Heeger. Solitons in Polyacetylene. *Phys. Rev. Lett.*, 42:1698–1701, 1979.

[9] Markus Konig, Steffen Wiedmann, Christoph Brune, Andreas Roth, Hartmut Buhmann, Laurens W. Molenkamp, Xiao-Liang Qi, and Shou-Cheng Zhang. Quantum spin hall insulator state in HgTe quantum wells. *Science*, 318(5851):766–770, 2007.

[10] B. Andrei Bernevig, Taylor L. Hughes, and Shou-Cheng Zhang. Quantum spin hall effect and topological phase transition in HgTe quantum wells. *Science*, 314(5806):1757–1761, 2006.

[11] Ivan Knez and Rui-Rui Du. Quantum spin hall effect in inverted InAs/GaSb quantum wells. *Frontiers of Physics*, 7(2):200–207, 2012.

[12] Haijun Zhang, Chao-Xing Liu, Xiao-Liang Qi, Xi Dai, Zhong Fang, and Shou-Cheng Zhang. Topological insulators in Bi_2Se_3, Bi_2Te_3 and Sb_2Te_3 with a single dirac cone on the surface. *Nat Phys*, 5(6):438–442, 2009.

[13] M. Zahid Hasan and Joel E. Moore. Three Dimensional Topological Insulators. *Annual Review of Condensed Matter Physics*, 2(1):55–78, 2011.

[14] Stephan Roche Ortmann, Frank and Sergio O. Valenzuela. *Topological Insulators: Fundamentals and Perspectives*. John Wiley & Sons, 2015.

[15] Xiao-Liang Qi and Shou-Cheng Zhang. Topological insulators and superconductors. *Rev. Mod. Phys.*, 83:1057–1110, 2011.

[16] András Pályi János Asbóth, László Oroszlány. A Short Course on Topological Insulators: Band-structure topology and edge states in one and two dimensions. 2015.

[17] Alexei Kitaev. Periodic table for topological insulators and superconductors. *AIP Conference Proceedings*, 1134(1):22–30, 2009.

[18] Alexander Altland and Martin R. Zirnbauer. Nonstandard symmetry classes in mesoscopic normal-superconducting hybrid structures. *Phys. Rev. B*, 55:1142–1161, 1997.

[19] Shinsei Ryu, Andreas P Schnyder, Akira Furusaki, and Andreas W W Ludwig. Topological insulators and superconductors: tenfold way and dimensional hierarchy. *New Journal of Physics*, 12(6):065010, 2010.

[20] Liang Fu and C. L. Kane. Topological insulators with inversion symmetry. *Phys. Rev. B*, 76:045302, 2007.

[21] Georg W. Winkler, Alexey A. Soluyanov, and Matthias Troyer. Smooth gauge and Wannier functions for topological band structures in arbitrary dimensions. *Phys. Rev. B*, 93:035453, 2016.

[22] M. Z. Hasan and C. L. Kane. Colloquium: Topological insulators. *Rev. Mod. Phys.*, 82:3045–3067, 2010.

[23] Raphael Leone. The geometry of (non)-Abelian adiabatic pumping. *Journal of Physics A: Mathematical and Theoretical*, 44(29):295301, 2011.

[24] C. Lacroix, P. Mendels, and F. Mila. *Introduction to Frustrated Magnetism: Materials, Experiments, Theory*. Springer Series in Solid-State Sciences. Springer, 2011.

[25] Wladimir A. Benalcazar, B. Andrei Bernevig, and Taylor L. Hughes. Electric multipole moments, topological multipole moment pumping, and chiral hinge states in crystalline insulators. *Phys. Rev. B*, 96:245115, 2017.

[26] Yu. M. Makeenko. Brief introduction to Wilson loops and large N. *Physics of Atomic Nuclei*, 73(5):878–894, 2010.

[27] Yuri Makeenko. *Methods of Contemporary Gauge Theory*. Cambridge University Press, 2002.

[28] R. G. Dias A. M. Marques. Generalization of Zak's phase for lattice models with non-centered inversion symmetry axis. 2017.

[29] J. Zak. Berry's phase for energy bands in solids. *Phys. Rev. Lett.*, 62:2747–2750, 1989.

[30] R. A. Webb, S. Washburn, C. P. Umbach, and R. B. Laibowitz. Observation of $\frac{h}{e}$ Aharonov-Bohm Oscillations in Normal-Metal Rings. *Phys. Rev. Lett.*, 54, 1985.

[31] Fernando L. J. Vos, Daniel Aalberts, and W Saarloos. Su-Schrieffer-Heeger model applied to chains of finite length. 53:14922–14928, 1996.

[32] R. G. Dias and J. D. Gouveia. Origami rules for the construction of localized eigenstates of the Hubbard model in decorated lattices. *Scientific Reports*, 5:16852, 2015.

[33] P. Delplace, D. Ullmo, and G. Montambaux. Zak phase and the existence of edge states in graphene. *Phys. Rev. B*, 84:195452, 2011.

[34] C. Weeks and M. Franz. Topological insulators on the Lieb and perovskite lattices. *Phys. Rev. B*, 82:085310, 2010.

[35] Wei-Feng Tsai, Chen Fang, Hong Yao, and Jiangping Hu. Interaction-driven topological and nematic phases on the Lieb lattice. *New Journal of Physics*, 17(5):055016, 2015.

[36] J.D. Gouveia and R.G. Dias. Magnetic phase diagram of the Hubbard model in the Lieb lattice. *Journal of Magnetism and Magnetic Materials*, 382:312 – 317, 2015.

[37] J.D. Gouveia and R.G. Dias. Spin and charge density waves in the Lieb lattice. *Journal of Magnetism and Magnetic Materials*, 405:292 – 303, 2016.

[38] Rui Wang, Qian Qiao, Bin Wang, Xiu-Huan Ding, and Yi-Fu Zhang. The topological quantum phase transitions in Lieb lattice driven by the Rashba SOC and exchange field. *The European Physical Journal B*, 89(9):192, 2016.

[39] Rui Chen and Bin Zhou. Finite size effects on the helical edge states on the Lieb lattice. *Chinese Physics B*, 25(6):067204, 2016.

[40] M. Niţă, B. Ostahie, and A. Aldea. Spectral and transport properties of the two-dimensional Lieb lattice. *Phys. Rev. B*, 87:125428, 2013.

[41] Liu Zheng, Liu Feng, and Wu Yong-Shi. Exotic electronic states in the world of flat bands: From theory to material. *Chinese Physics B*, 23(7):077308, 2014.

[42] S. J. Barnett. On the Theory of Diamagnetism. *Phys. Rev.*, 25:835–840, 1925.

[43] J. D. Gouveia, I. A. Maceira, and R. G. Dias. Evolution of localized states in Lieb lattices under time-dependent magnetic fields. *Phys. Rev. B*, 94:195132, 2016.

[44] Luuk J. P. Ament, Michel van Veenendaal, Thomas P. Devereaux, John P. Hill, and Jeroen van den Brink. Resonant inelastic X-ray scattering studies of elementary excitations. *Reviews of Modern Physics*, 83(2), 2011.

[45] E. Meyer M. Heinrich O. Zilberberg A. Szameit M. Kremer, I. Petrides. Non-quantized square-root topological insulators: a realization in photonic Aharonov-Bohm cages. 2018.

[46] A. A. Lopes and R. G. Dias. Interacting spinless fermions in a diamond chain. *Phys. Rev. B*, 84:085124, 2011.

[47] Zsolt Gulácsi, Arno Kampf, and Dieter Vollhardt. Exact Many-Electron Ground States on the Diamond Hubbard Chain. *Phys. Rev. Lett.*, 99:026404, 2007.